Ore Geology Reviews 149 (2022) 105095

Contents lists available at ScienceDirect

Ore Geology Reviews

journal homepage: www.elsevier.com/locate/oregeorev

The geological setting of the indium-rich Baal Gammon and Isabel Sn-Cu-Zn deposits in the Herberton Mineral Field, Queensland, Australia

Avish A. Kumar *, Ioan V. Sanislav, Paul H.G.M. Dirks

Economic Geology Research Centre (EGRU) and Department of Earth and Environmental Sciences, James Cook University, Townsville, Queensland, Australia

ARTICLE INFO

Keywords:
Herberton Mineral Field
Critical Metals
Indium
Tin
Mossman Orogen

ABSTRACT

Base metal mineralization at the Baal Gammon and Isabel deposits of the Herberton Mineral Field (HMF) is hosted in metamorphosed greywacke beds in the Hodgkinson Formation, which were intruded by granite, porphyry dykes and overlain by volcanic rocks of the Kennedy Igneous Association during the Carboniferous and Permian. The tin mineralization at the Baal Gammon deposit is hosted by a silicified, chlorite-altered, quartz-feldspar porphyry (UNA Porphyry). The tin mineralization at the Isabel deposit is in polymetallic veins hosting disseminated cassiterite. Polymetallic sulfides (Cu-Zn) and indium (In) mineralization at both deposits overprint the tin mineralization. Chalcopyrite, sphalerite, and stannite host indium in the polymetallic sulfide assemblage at both deposits. Based on overprinting relationships, the timing of tin mineralization is related to the magmatic activity at ca. 320 Ma, whereas the sulfide and indium mineralization are most likely associated with the emplacement of porphyry dykes at ca. 290 Ma. The overall magmatic activity in the HMF spreads between ca. 365 and 280 Ma, with peaks at ca. 337, 322, 305, and 285 Ma. The change from tin mineralization at ca. 320 Ma to sulfide and indium mineralization at ca. 290 Ma indicates a transition from a compressive to an extensional tectonic regime.

1. Introduction

Indium is one of the critical metals with a substantial increase in demand over the last two decades, because of its increased usage in the production of flat panel displays, touchscreens, photovoltaic cells, and fiber optic technology (Fontana et al., 2021). Economic concentrations of In mineralization are found in various types of deposits, including volcanogenic massive sulfide (VMS), sediment-hosted base-metal, epithermal, skarn, porphyry, and granite-related deposits (Schwarz-Schampera and Herzig, 2002; Werner et al., 2017). Polymetallic tin deposits, particularly those with a magmatic-hydrothermal origin that host base-metal mineralization, can be significantly enriched in In (Korges et al., 2020; Voudouris et al., 2022).

The HMF forms the northern part of multiple tin provinces situated along the Tasman Fold Belt (or the Tasmanides of Walshe et al., 2011). The occurrence of tin in the mineral field is associated with polymetallic mineralization that contains high-grade In. Tin, base-metals, and In mineralization are commonly associated with fractionated granites in the fold belt (Walshe et al., 2011).

Three major tin fields have been described from the Tasman Fold Belt, including the cassiterite (SnO_2) deposits in Tasmania (Collins and Williams, 1986), the Ardlethan tin field in New South Wales (Ren et al., 1995), and the HMF in Queensland (Pollard, 1988). Cassiterite from the Tasmanian tin field has yielded U-Pb mineralization ages of ca. 391 and 359 Ma (Denholm et al., 2021), whereas cassiterite from the New South Wales tin field has yielded a younger U-Pb mineralization age of ca. 246 Ma (Carr et al., 2020). The U-Pb zircon ages from granites in both tin fields are similar to the related U-Pb cassiterite ages (Carr et al., 2020; Schaltegger et al., 2005), thus zircon ages can provide good estimates of tin mineralization related to particular magmatic activities. There is limited age data available from HMF and consequently the relationship between tin, polymetallic veins and In mineralization is unclear.

Tin was discovered in the HMF in 1875, and mining began around 1880 (Dash et al., 1991). By 1971, most mining companies in the HMF were exploring for polymetallic systems containing Zn, Pb, W, Au, Bi, Cu, Ag, In, and Cd (Kositcin et al., 2009; Clarke and Chang, 2017). These polymetallic deposits are associated with microgranites, pegmatite veins, greisen, skarn, volcanic rocks, and meta-basalt (Clarke and Chang, 2017). The Baal Gammon and Isabel deposits within the HMF are the only deposits with a defined In resource and are the focus of this paper.

* Corresponding author.
E-mail address: avish.kumar@my.jcu.edu.au (A.A. Kumar).

https://doi.org/10.1016/j.oregeorev.2022.105095
Received 7 April 2022; Received in revised form 1 September 2022; Accepted 3 September 2022
Available online 6 September 2022

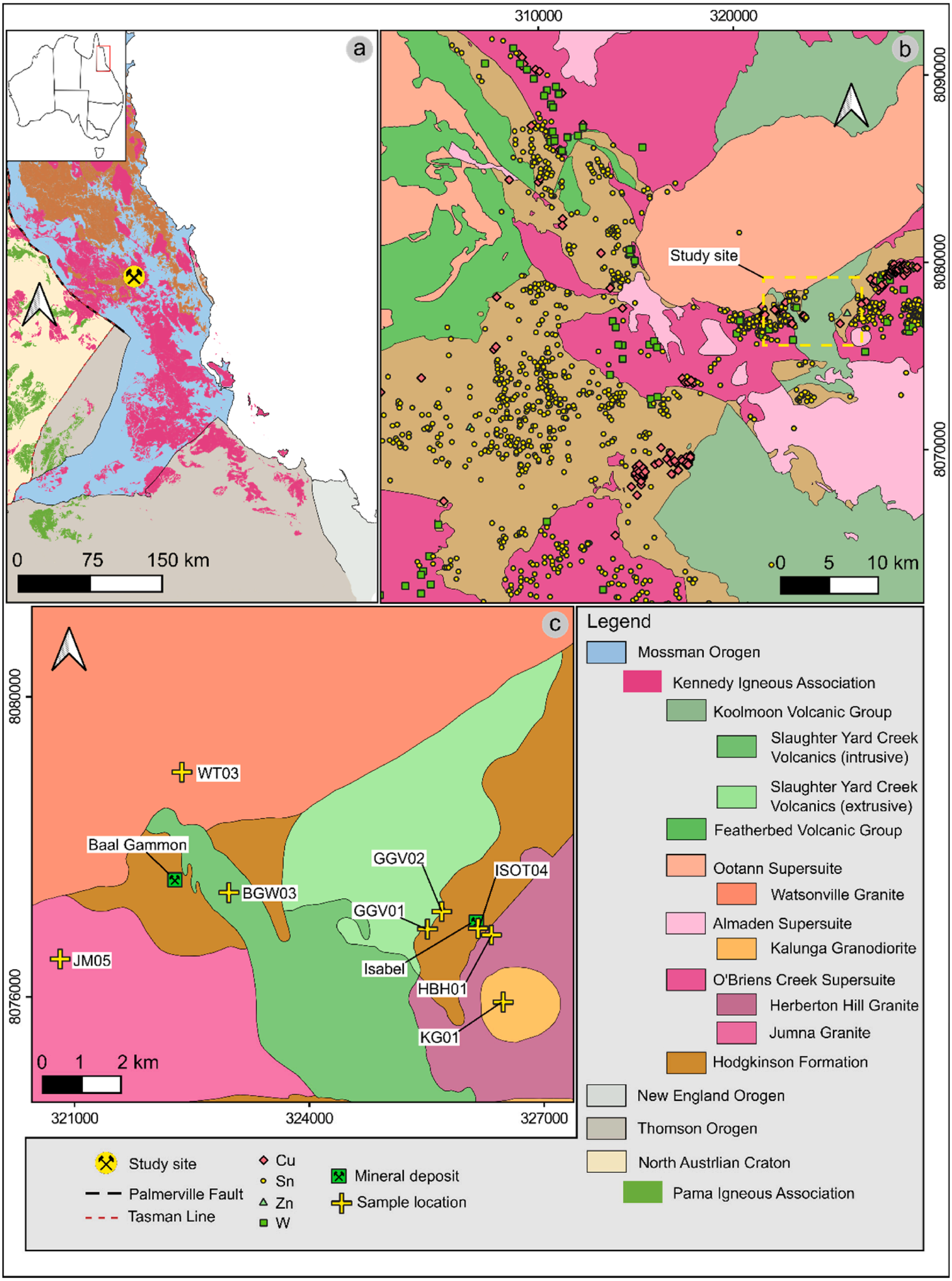

Fig. 1. Simplified geological maps of: (a) north Queensland; (b) the Herberton Mineral Field; and (c) the Baal Gammon and Isabel deposits.

The deposits are ~5 km apart and located northwest of the Herberton township (Fig. 1). This paper provides a geological framework for the Baal Gammon and Isabel deposits, age estimates for mineralization events, and further improves the tectonic setting for HMF from Cheng et al. (2018) and Champion (2016).

2. Geological setting

The northeast margin of the Tasmanides formed via accretion during the Cambrian to the Triassic. It contains important metallogenic domains that host base, precious, and critical metals (Edgar et al., 2022a,b, Glen, 2005, 2013; Rosenbaum, 2018). In northeast Australia, the Tasmanides comprise the Phanerozoic Mossman and Thomson Orogens which are separated from the Mesoproterozoic Georgetown inlier by the Palmerville Fault (Fergusson et al., 2007; Murgulov et al., 2007; Rosenbaum, 2018; Fig. 1). Devonian to Cenozoic sedimentary sequences cover most of the Thompson Orogen (Fergusson et al., 2013) and, together with the adjacent North Australia Craton, was intruded by Silurian to Devonian granites included in the Pama Igneous Association. The suite consists predominantly of I-type granites emplaced between ca. 434 and 382 Ma (Bain and Draper, 1997; Henderson et al., 2013).

The Mossman Orogen largely consists of the Hodgkinson Group that is intruded by granites of the Kennedy Igneous Association (Henderson et al., 2013; Fig. 1). The group consists of shallow-marine limestone (Chillagoe Formation) and turbidites intercalated with mélange deposits (Barron-Palmer Formation; Withnall and Henderson, 2012), which in the western part of the group were interpreted as being deposited on an abyssal fan (Henderson et al., 2013). The maximum depositional age of the group has been variably estimated at ca. 482, 463, 454, and 370 Ma, based on the age of detrital zircons (Henderson et al., 2013; Kositcin and Bultitude, 2015), but its minimum age is constrained by the age of the Kennedy Igneous Association.

The Kennedy Igneous Association is composed of Carboniferous to Permian granites, high-level intrusive, and volcanic rocks. The granites have been grouped in suites and supersuites, based on petrological similarities (White et al., 2001). This grouping of the granites is based on various assumptions, and most batholiths are composites of multiple intrusions. Supersuites identified in the HMF include, from oldest to youngest, the O'Briens Creek, Ootan and Almaden supersuites (Fig. 1). Volcanic units near the study site consist of the Featherbed and Koolmoon volcanics.

The O'Briens Creek Supersuite is highly fractionated, and includes the Herberton Hill and Jumna granites (Champion, 1991; Fig. 1). The supersuite typically consists of pink to yellow alkali feldspar granite associated with granophyre, microgranite, topaz-bearing aplite and silexite, which reflects the fractionated nature of this unit (Johnston and Black, 1986). Dating by Cheng et al. (2018) has constrained the age of this unit to ca. 335–317 Ma.

The Ootann Supersuite is widespread in HMF (Champion, 1991), and is represented by the Carboniferous (ca. 310–302 Ma) Watsonville Granite in the study area (Cheng et al., 2018; Fig. 1). The granite is medium- to coarse-grained and commonly contains veins of aplite and patches of pegmatite (Blake, 1972).

The Almaden Supersuite consists of granodiorite with minor diorite, and it includes the Kalunga Granodiorite south of the Isabel deposit (Fig. 1). The granodiorite is not mineralized and contains medium-grained quartz, zoned oligoclase-andesine, turbid orthoclase, and biotite that defines a hypidiomorphic granular texture (Sheraton and Labonne, 1978).

The Featherbed Volcanics have been divided into the Old and Young Featherbeds. The Old Featherbed Volcanics yield ages of ca. 325–317–Ma (Cheng et al., 2018), which consists of dacitic to rhyolitic ignimbrite and minor andesitic tuff (Cheng et al., 2018; Mackenzie, 1993). The age of the Young Featherbed Volcanic unit has been constrained at ca. 310–275 Ma (Cheng et al., 2018). The unit consists of porphyritic rhyolite, rhyolitic ignimbrite, volcanic breccia, microgranite, and minor dacite (Cheng et al., 2018; Sheraton and Labonne, 1978).

The Koolmoon Volcanic Group consists of the Walsh Bluff, Glen Gordon, and Slaughter Yard Creek Volcanics (Donchak and Bultitude, 1998). The group consists of tuff, tuffaceous sandstone and siltstone, felsic lava flows, and agglomerate (Blake, 1972). Despite being grouped as volcanics, the ca. 284 Ma Slaughter Yard Creek Volcanics contain intrusive rocks that consist of quartz-feldspar porphyry and felsic dykes (Cheng et al. 2018; Fig. 1).

Table 1
Summary of LA-ICP-MS analyses of chalcopyrite, pyrrhotite, and sphalerite from the Baal Gammon deposit.

Mineral		Cu	Zn	In	Sn
Chalcopyrite	Min		727	1071	1323
(n = 15)	Max		1896	1727	2354
	Mean		1135	1244	1610
	S.D.		371	156	293
Pyrrhotite	Min	2.7	1.6	0.01	0.3
(n = 15)	Max	5210	4328	1242	3359
	Mean	2437	1106	288	1086
	S.D.	2077	1637	439	1342
Sphalerite	Min	4951		3009	106
(n = 15)	Max	60,144		6795	13,013
	Mean	23,793		4041	1434
	S.D.	16,126		1011	3253

Table 2
Summary of LA-ICP-MS analyses of chalcopyrite, pyrrhotite, and sphalerite from the Isabel deposit.

Mineral		Cu	Zn	In	Sn
Chalcopyrite	Min		355	573	484
(n = 15)	Max		16,881	857	7841
	Mean		2924	705	1194
	S.D.		4270	90	1853
Pyrrhotite	Min	1.7	13.1	0.09	0.9
(n = 15)	Max	59,256	13,644	2182	4336
	Mean	8453	1709	442	508
	S.D.	16,594	3419	595	1086
Sphalerite	Min	984		1303	3
(n = 15)	Max	19,622		1565	1321
	Mean	2866		1501	143
	S.D.	4736		63	338

3. Methods

Indium-rich sulfides ore at the Baal Gammon and Isabel deposits were identified from diamond-drill core assay data. Eleven Baal

Table 3
Summary of $^{206}Pb/^{238}U$ zircon ages for the Baal Gammon and Isabel deposits and regional granites and volcanic units.

Sample #	Unit	$^{206}Pb/^{238}U$ Weighted Mean age/MDA* (Ma, and error as 2σ)	MSWD	N
BG01	Slaughter Yard Creek Volcanics	289 ± 1	0.85	47
BG02	Slaughter Yard Creek Volcanics	288 ± 1	1.23	42
BGW03	Slaughter Yard Creek Volcanics	288 ± 1	0.70	34
BGOT009	UNA Porphyry	333 ± 2	1.45	21
GGV01	Slaughter Yard Creek Volcanics	293 ± 1	1.48	12
GGV02	Slaughter Yard Creek Volcanics	326 ± 1	1.15	19
HBH01	Herberton Hill Granite	339 ± 2	1.51	11
JM05	Jumna Granite	365 ± 2	0.70	9
KG06	Kalunga Granodiorite	315 ± 2	1.41	13
WT03	Watsonville Granite	285 ± 1	1.01	20
ISOT09	Slaughter Yard Creek Volcanic	292 ± 1	0.61	32
ISOT04	Hodgkinson Formation	457*		

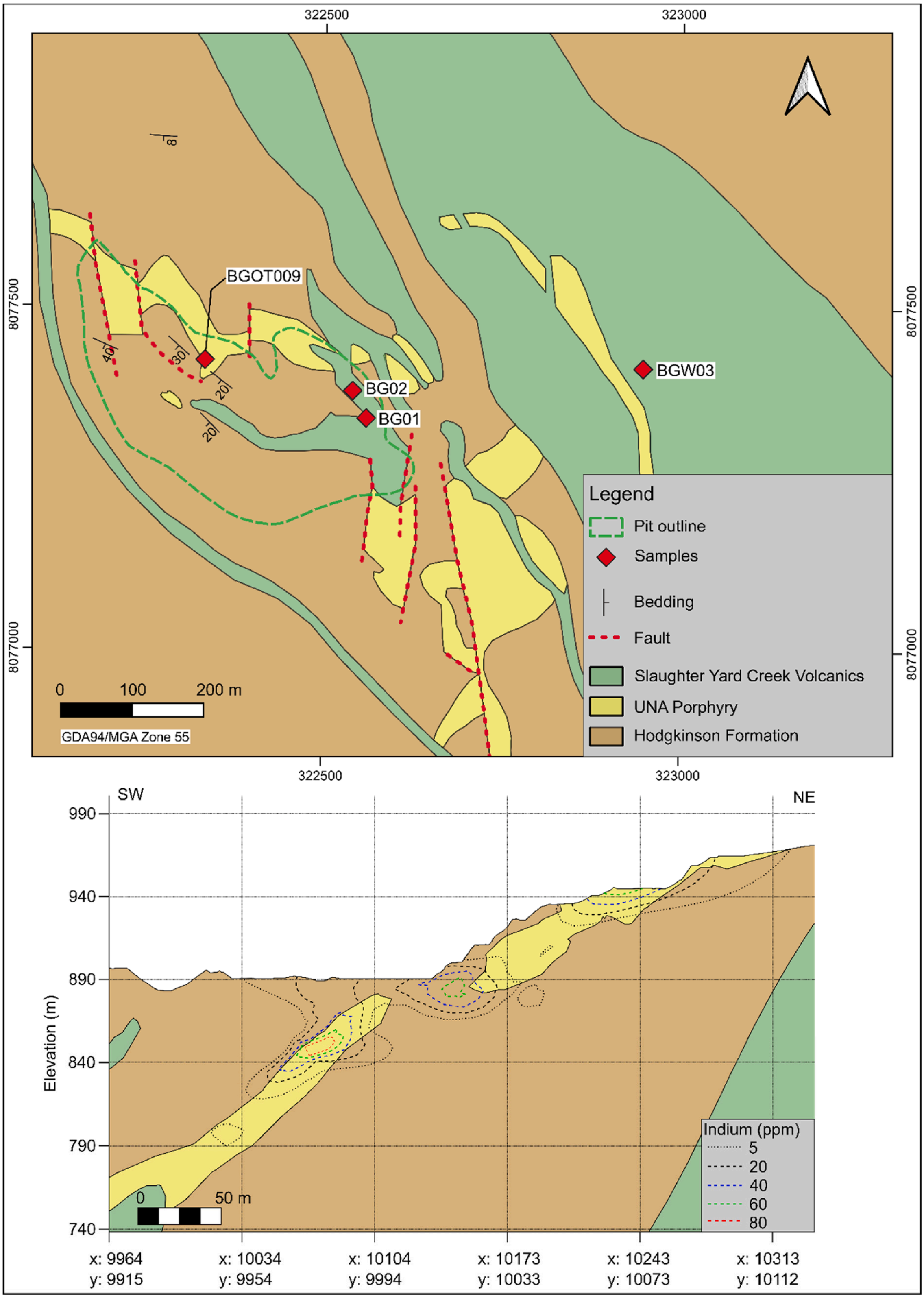

Fig. 2. Geological map of the Baal Gammon deposit and a SW-NE cross-section through the open pit.

Gammon and eleven Isabel quarter diamond-drill cores from the identified In-rich zones were obtained from the Geological Survey of Queensland for petrographic, SEM, and LA-ICP-MS analyses. Petrography was conducted on all the samples; SEM on four Baal Gammon, and three Isabel samples; and LA-ICP-MS on two Baal Gammon, and two Isabel samples.

The petrographic analyses and interpreted mineral paragenesis are based on transmitted and reflected light microscope, and scanning electron microscopy. A Hitachi SU5000 SEM, at the Advanced Analytical Centre of the James Cook University, was used for imaging by

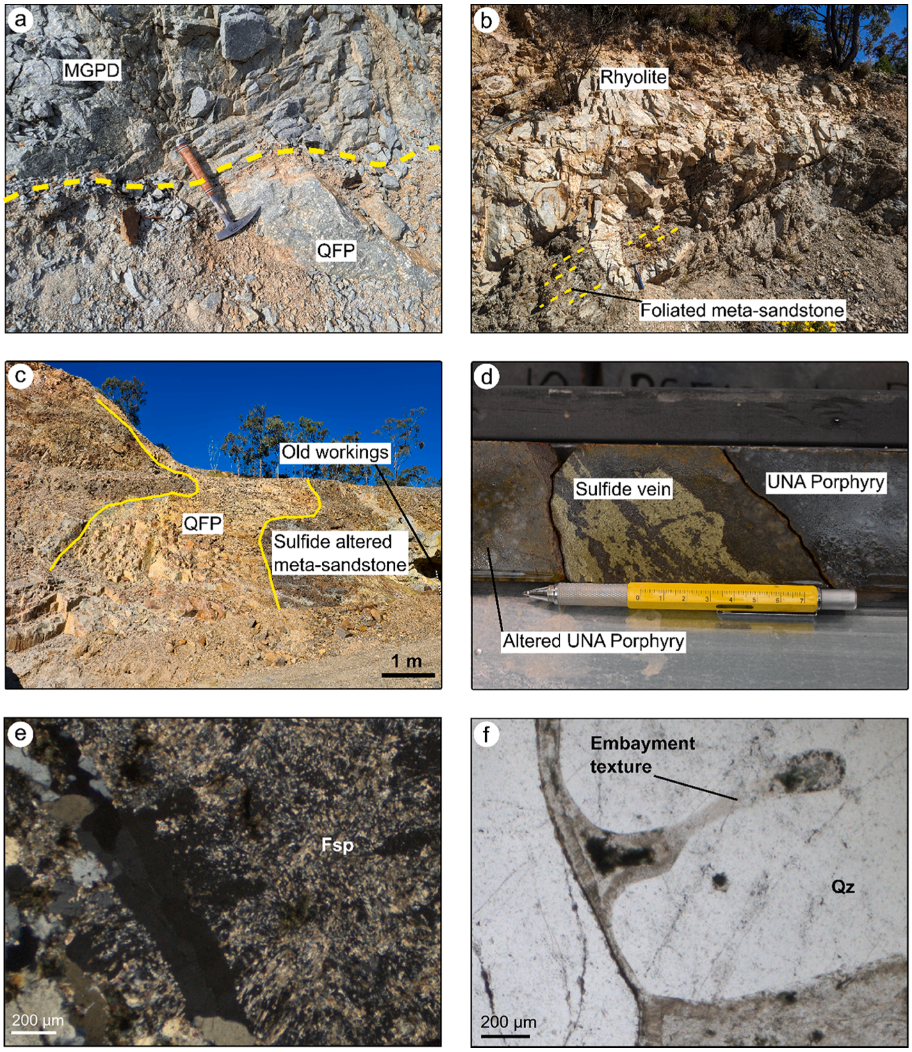

Fig. 3. Field photographs (a-c), diamond-drill core (d) and microscope images (e-f) of samples from the Baal Gammon deposit: (a) the contact between MGPD and QFP; (b) low level rhyolite intrusion; (c) sulfide-altered meta-sandstone in contact with a QFP dyke; (d) diamond-drillhole core showing sulfide vein crosscutting the UNA Porphyry; (e) sericite alteration of feldspar (Fsp) in the UNA Porphyry (crossed-nicols polarized light photomicrograph); and (f) embayed quartz (Qz) in the UNA Porphyry (crossed-nicols polarized light photomicrograph).

backscatter electron (BSE), and mineral identification and compositional mapping by energy dispersive spectroscopy (EDS).

Spot analyses for elements concentration on sulfide phases were conducted on a Thermo iCap-TQ ICP-MS instrument coupled to an Analyte G2 Excimer Laser Ablation system with the parameters: 2 J/cm^2 laser energy density; 5 Hz laser repetition rate; and 40 µm laser spot size. The standards, NIST610, MASS-1, and GSE-1, were analysed, and the data was reduced using the Iolite software (Paton et al., 2011). Summaries of the results are presented in Tables 1 and 2.

Twelve samples consisting of intrusive dykes, meta-sedimentary, granitic, and volcanic rocks were selected for U-Pb zircon dating (Table. 3). From the Baal Gammon deposit (Fig. 2), samples were taken from the UNA Porphyry (BGOT009), quartz-feldspar porphyry (BG01), medium-grained porphyry (BG02) and shallow-level intrusive rhyolitic dyke (BGW03). From the Isabel deposit, samples were taken from non-mineralized brecciated meta-sedimentary rock (ISOT04), and from a quartz-feldspar porphyry dyke (QFPI) that intrudes the meta-sedimentary rocks next to the deposit (ISOT09). From the regional granite intrusions, samples were taken from the Herberton Hill Granite (HBH01), Jumna Granite (JM05), Kalunga Granodiorite (KG06), and Watsonville Granite (WT03). In addition, two samples were collected from the Slaughter Yard Creek Volcanics (GGV01 and GGV02).

The samples were crushed to obtain fresh chips that were milled and sieved to grain sizes of ≤500 µm. Heavy minerals were separated from the sieved samples using standard magnetic, and heavy liquid separation techniques. Zircons were hand-picked from the heavy mineral separates, mounted in epoxy resin, and polished to near mid-section exposure. To illustrate zoning patterns, the polished zircons were imaged with a cathodoluminescence detector attached to a Jeol JSM5410LV scanning electron microscope.

The zircons were analysed for U-Pb isotopes with an Analyte G2 Excimer Laser Ablation system coupled to a Thermo iCap-RQ ICP-MS instrument. The ablation was carried out with a laser with an energy density of 2 J/cm^2 at a rate of 5 Hz on a spot size of 30 µm. All the samples were imaged and dated at the Advanced Analytical Centre, James Cook University, Townsville.

Isotope data were reduced using the Iolite software (Fisher et al., 2017), and age calculations were done with IsoplotR (Vermeesch, 2018). The weighted average ages were calculated using the $^{206}Pb/^{238}U$ isotope system. For igneous samples, 50 to 60 zircon spots were analysed and only analyses with <5% discordance were used for age calculations. Only analyses with <10% discordance were used to determine the maximum depositional age of detrital zircons. The Plešovice zircon (ID-TIMS $^{206}Pb/^{238}U$ age of 337.13 ± 0.37 Ma; Sláma et al., 2008) was used as the primary standard for downhole fractionation corrections. The secondary zircon standards used are Zircon GJ-1 (ID-TIMS $^{207}Pb/^{206}Pb$ age of 608 ± 2 Ma and $^{206}Pb/^{238}U$ age of 602 ± 0.4 Ma; Jackson et al., 2004; Horstwood et al., 2016), and 91500 ($^{207}Pb/^{206}Pb$ age of 1067 ± 1.5 Ma and $^{206}Pb/^{238}U$ age of 1064 ± 0.65 Ma; Wiedenbeck et al., 1995; Horstwood et al., 2016). The GJ1 and 91500 zircons yielded a weighted mean $^{206}Pb/^{238}U$ age of 605 ± 1 Ma (n = 182) and 1072 ± 1 Ma (n = 182), respectively. The calculated concordia ages for the secondary zircon standards were 604 ± 1 Ma (GJ1, n = 182) and 1071 ± 1 Ma (91500, n = 182). A summary of the results is presented in Table 3 with errors reported at 2σ.

4. The geology of the Baal Gammon and Isabel deposits

4.1. The Baal Gammon deposit

4.1.1. The host rocks

The Baal Gammon Sn-Cu-Zn-In deposit is located at the contact between meta-sandstone assigned to the Hodgkinson Formation and the UNA Porphyry (Fraser, 1972; Fig. 2). The formation constitutes the oldest geological unit in the area, and consists of cross-bedded fine- to coarse-grained meta-sandstone that dips gently (~20°) towards the south to southwest. The formation is intruded and hydrothermally altered by the tin-bearing, UNA Porphyry, barren quartz veins, and quartz-feldspar porphyry dykes mapped as the Slaughter Yard Creek Volcanics (Donchak and Bultitude, 1998). Fraser (1972) has observed the presence of andalusite in the meta-sandstone near the UNA Porphyry, but no andalusite was identified during this study. The meta-sandstone in the open pit at Baal Gammon is strongly jointed and fractured, altered, and silicified, with muscovite growth parallel to joints and fractures.

4.1.2. Intrusive rocks

The UNA Porphyry is granitic in composition, and intrudes the Hodgkinson Formation as an irregularly shaped dyke dipping shallowly to moderately south (Fig. 2b). Its patchy appearance in outcrop is due to its irregular shape, and an orientation that is subparallel to the topography. The porphyry and Hodgkinson Formation are crosscut by a series of veins of biotite, chlorite, muscovite and garnet, and a series of steeply dipping, NNW trending faults.

The UNA Porphyry at the Baal Gammon open pit surrounding hills is highly altered, and has a vuggy texture. The less altered section of the porphyry is composed of quartz (50%), alkali feldspar (10%), plagioclase (5%), biotite, chlorite, garnet, and sulfides, with a granophyric groundmass. The subhedral, porphyritic quartz crystals have embayments of fine-grained material similar in composition to the surrounding matrix, and commonly display a spongy texture (Fig. 3). The embayment textures may have formed during decompression and ascent of the porphyritic body, when the quartz crystals were partially dissolved (Chang and Meinert, 2004). Most of the plagioclase and alkali feldspar are altered to sericite, and biotite is partly altered to chlorite.

4.1.3. Volcanic rocks

The Slaughter Yard Creek Volcanics near the Baal Gammon deposit forms shallow level dykes of variable thickness (Fig. 2), which are subvertical and trend NW. Three different dyke phases were identified based on texture, composition, and overprinting relationships. The oldest phase consists of a coarse-grained, quartz-feldspar porphyry (QFP) trending eastward (Fig. 3). The quartz-feldspar porphyry varies in thickness from a few meters in the western wall of the pit to almost ten meters in the eastern pit wall. It consists of up to 20 mm large phenocrysts of plagioclase and quartz, in a fine-grained groundmass of quartz, plagioclase, K-feldspar and minor biotite. The quartz phenocrysts have an irregular shape and are commonly embayed. The second phase consists of a medium-grained porphyritic dyke (MGPD; Fig. 3a) composed of plagioclase, quartz, K-feldspar, biotite, and chlorite. Near contacts, the MGPD contains small fragments of phenocrysts of coarse-grained quartz and plagioclase like that in the QFP. This suggests that the MGPD postdated the QFP, and fragments of the QFP were incorporated in the MGPD during emplacement. The MGPD is exposed only on the eastern side in the pit where it trends SE. Biotite and chlorite are secondary alteration products in the groundmass. The youngest phase of the Slaughter Yard Creek Volcanics consists of shallow intrusive rhyolite dykes in the northeastern part of the deposit (Fig. 3b).

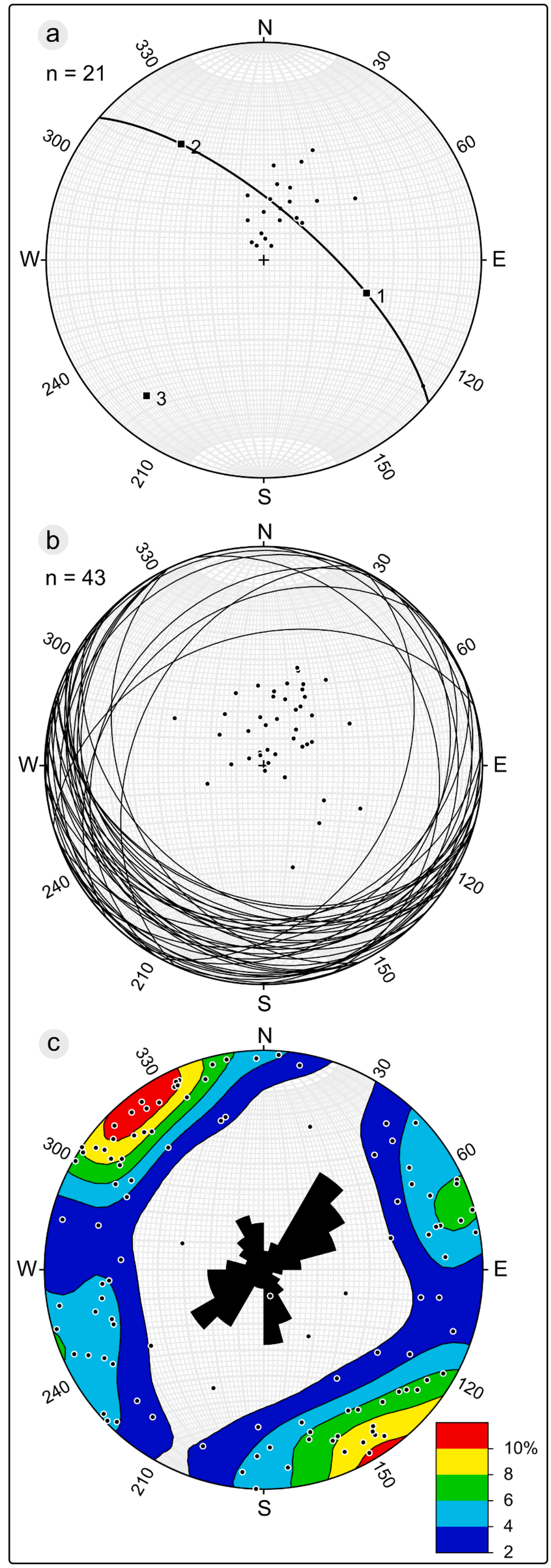

Fig. 4. Stereonet plots of structural elements measured at the Baal Gammon deposit includes: (a) poles to bedding measured in the meta-sandstone; (b) poles and planes of bedding parallel shears; and (c) poles to fractures and rose diagram of the fracture planes.

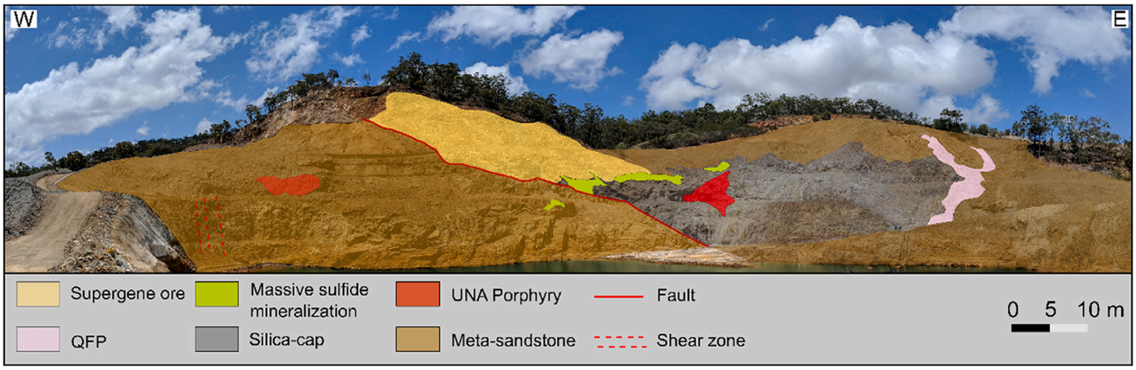

Fig. 5. Image of the northern pit wall of the Baal Gammon deposit with an overlay of the geological units.

4.1.4. Structures

The meta-sedimentary rocks in the Baal Gammon area dip to the SW and are open folded with a fold axis that plunges gently towards 220° (Fig. 4). Apart from bedding, no tectonic foliation was recognized. The UNA Porphyry is displaced by a series of moderately eastward dipping and NNW trending reverse faults (Fig. 5). In addition, the meta-sedimentary rocks are affected by bedding-parallel fractures and shears that dip 20–40° SW (Fig. 4). All rock units display these fractures and shears, which are accompanied by a set of conjugate sub-vertical joints trending NE and NNW.

4.1.5. Mineralization and distribution of indium at the Baal Gammon deposit

Based on crosscutting relationships and alteration characteristics, the primary mineralization in the Baal Gammon deposit can be subdivided into an early, tin oxide stage (stage I), and a later massive sulfide stage (stage II). Stage I is characterized by strong silicification of the meta-sandstone developed as a silica cap surrounding the UNA Porphyry, and in deeper parts of the UNA Porphyry (Fig. 5), sericite alteration (Fig. 3e), and cassiterite precipitation in the UNA Porphyry. The feldspar in the porphyry is sericite-altered (Fig. 3e), and cassiterite grains within the porphyry occur as 100–600 μm, zoned, euhedral crystals. Stage II mineralization is characterized by massive sulfides, sulfide veins (Fig. 3d), and breccia infill. Massive sulfides and mineralized brecciated meta-sandstone are present along the contact with the UNA Porphyry. The porphyry and the meta-sandstone are also crosscut by sulfide veins (Fig. 3d).

A supergene alteration cap can be observed in the open pit and the surrounding rocks (Fig. 5). The supergene cap has a wedge shape and developed above the mineralized meta-sandstone. It is dominated by iron oxides and silica, with an infill of malachite and azurite in a vuggy to honeycomb texture. Fine-grained covellite occurs as infill surrounding azurite. Near the deposit, the supergene mineralization is positioned above an east dipping fault (Fig. 5).

The distribution of In in the Baal Gammon deposit is closely related to the UNA Porphyry and the massive sulfide mineralization. The highest grades were recorded in semi-massive sulfide veins within the porphyry, or along the contact between the porphyry and the Hodgkinson Formation (Fig. 2b). The resource models indicate an average grade of ~63 ppm In. Element-element correlations of ore analysed from diamond-drill core at Baal Gammon (Fig. 6) show a strong positive correlation between In and Cu ($r = 0.9$) and Ag ($r = 0.8$) and a moderate correlation with Fe ($r = 0.6$), Bi ($r = 0.5$) and Zn ($r = 0.4$). The Cu-rich parts of the deposit (>0.1% Cu) have an average grade of ~40 ppm In reaching up to 1140 ppm In in sulfides along the UNA Porphyry and Hodgkinson Formation contact. High-grade (>50 ppm) Ag ore contains an average of ~110 ppm In, and the highest In grades were observed within the porphyry or at the contact of the meta-sediments with the porphyry. Indium displayed a weak positive correlation with Au ($r = 0.3$), As ($r = 0.2$), Pb ($r = 0.2$), Sb ($r = 0.3$), Sn ($r = 0.3$), W ($r = 0.3$), and Cd ($r = 0.3$). Apart from Sn, most of these metals are limited in tonnage and grade. For example, W forms high-grade thin (<10 mm) quartz veins within a vertical shear zone developed in the porphyry.

4.2. The Isabel deposit

4.2.1. Country rocks

The Pb-Zn-Ag mineralization at the Isabel deposit is hosted by the Hodgkinson Formation and intruded by dolerite, quartz-feldspar porphyry, and feldspar porphyry dykes (Fig. 7). The formation consist of poorly sorted, coarse- to fine-grained arkosic sandstone containing quartz-feldspar, lenses of siltstone and chert, and is variably iron-stained at the ground surface. The quartz grains are recrystallized with polygonal textures and undulose extinction. In drill core, the meta-sandstone below the iron staining is chlorite–sericite altered and appear dark green. The meta-sandstone host of the deposit is brecciated, with both fault breccia and hydrothermal breccia being present. The fault breccia is not mineralized and consists of angular meta-sedimentary clasts in a jigsaw-fit within a fine-grained quartz, feldspar, chlorite, and muscovite matrix. The hydrothermal breccia contains significant sulfide mineralization, with the angular clasts display a jigsaw-fit texture, with infilling fine-grained sulfide mineralization (Fig. 7c). The breccia has a gossan cap composed of iron oxide and clay. The Hodgkinson Formation is contact with the Herberton Hill Granite to the south (Fig. 7).

4.2.2. Igneous rocks

Igneous rocks near the Isabel deposit consist of the Herberton Hill Granite, Slaughter Yard Creek Volcanics, and porphyry dykes. The contact between the Herberton Hill Granite and country rocks trends NE, which are intruded by shallow level porphyry dykes assigned to the Slaughter Yard Creek Volcanics. The best exposed phase of the Herberton Hill Granite is a coarse-grained, pink, leucocratic monzogranite with traces of primary biotite and mica. The monzogranite is exposed at the southeastern end of the Isabel deposit (Fig. 7a), where it is moderately weathered with plagioclase and K-feldspar altered to clay, and iron oxides have formed at the boundary of quartz grains.

The porphyry dykes comprise feldspar porphyry, quartz-feldspar porphyry, and dolerite dykes. Only the quartz-feldspar porphyry (QFPI) and dolerite dykes are exposed at the ground surface. The QFPI consists of plagioclase altered to sericite and embayed quartz. The altered feldspar is surrounded by muscovite, and locally contains carbonates in vugs. The groundmass consists of fine-grained quartz, plagioclase and chlorite, and opaque minerals replacing feldspar and the groundmass. The groundmass has a granophyric texture and consists of quartz, altered feldspar and chlorite. The dolerite dyke is fine-grained and chlorite-sericite altered. It contains veins and late infill of vugs by fine-grained quartz, plagioclase, and carbonates; pyroxene and plagioclase have been altered to chlorite.

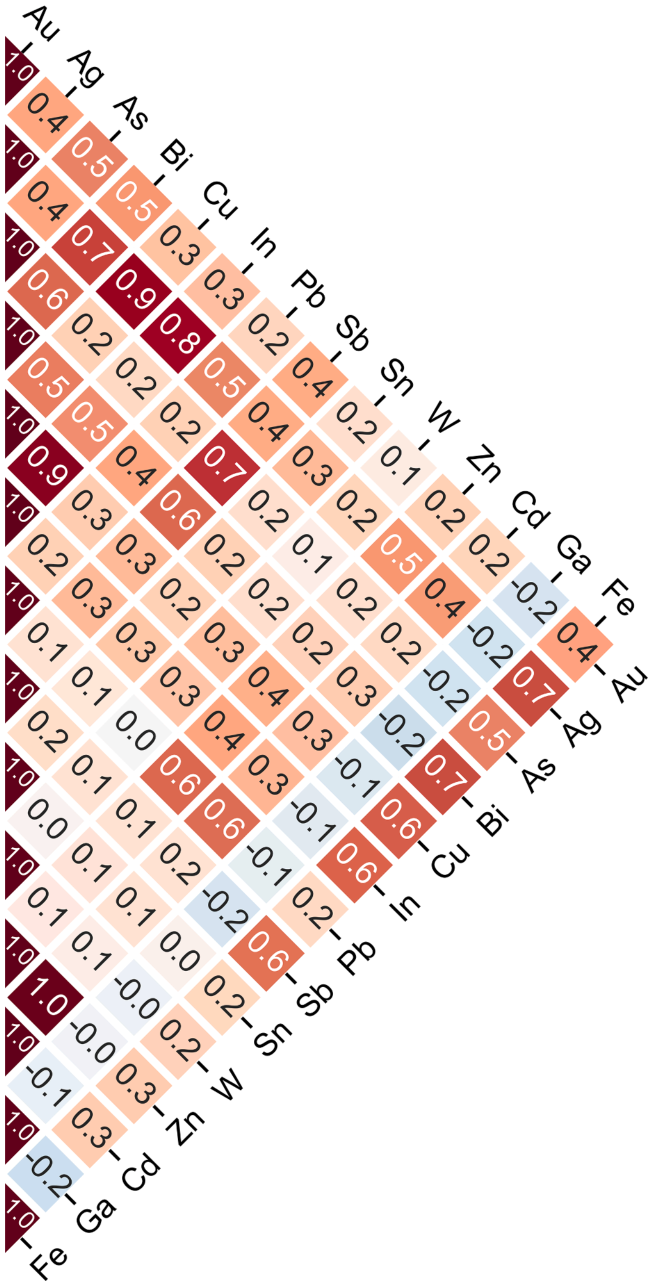

Fig. 6. Element-element correlation matrix for geochemical assay data from the Baal Gammon diamond-drill core. Approximately 1200 assays were taken for developing the correlation matrix from 380 diamond-drillholes and values above the detection limit were used.

The Slaughter Yard Creek Volcanics comprise shallow level intrusive and extrusive rock units. The extrusive components include breccia and welded tuff, interbedded with thinly bedded siltstone, and sandstone. The breccia is composed of angular sedimentary fragments that are up to 10 cm in size. These fragments consist of recrystallized quartz and muscovite in a matrix of silica, sericite, albite, and quartz. The welded tuff is light brown to gray-green in color and has a eutaxitic texture with vugs. The feldspar grains in the welded tuff are angular and have been replaced by chlorite; the quartz grains are rounded and preserve embayments. The siltstone and sandstone are creamy white in color and contain abundant angular quartz fragments. Field evidence suggests that the ore body was positioned close to the contact between the metasediments and the QFPI dyke (Fig. 7b).

4.2.3. *Structural setting*

The Hodgkinson Formation at the Isabel deposit dips 75° east, where it is faulted and intruded by porphyry and dolerite dykes. Robinson (1983) has recognized four sets of lineaments, interpreted as faults, striking at 327° (first generation), 45° (second generation), 275° (third generation), and 300° (fourth generation). The quartz feldspar porphyry and dolerite dykes are parallel to the first generation of lineaments (Fig. 7a). The second generation of lineaments are parallel to the contact between the monzogranite and host rocks. This lineament orientation correlates with the orientation of tin mineralization near the Isabel deposit. The areas of intersection between the first and fourth lineament generations is characterized by intense brecciation, and the deposition of lead–zinc sulfides ore (Robinson, 1983).

4.2.4. *Mineralization and distribution of indium at Isabel*

The Pb-Zn-Ag mineralization at Isabel consists of polymetallic veins and breccia hosted by the Hodgkinson Formation. Based on the composition of the sulfide minerals, the polymetallic veins recognized are here referred to as the Type I and Type II vein sets. The Type I veins consisting of disseminated cassiterite and sphalerite containing chalcopyrite inclusions, and are crosscut by chalcopyrite-pyrrhotite veins. The cassiterite grains are fractured and show early stages of alteration (Fig. 7e). The Type II veins consist of sphalerite, galena, and stannite. The galena forms idiomorphic crystals and shows triangular pits under reflected light. The sphalerite and quartz veins crosscut the galena, and the sphalerite contains stannite inclusions.

Resource models for the Isabel deposit indicate an average In grade of ~370 ppm (Red River Resources Limited., ASX announcements, 2020). The Sn- and Cu-rich parts of the deposit (>1% Cu, and >0.2% Sn) have an average In concentration of ~1140 ppm, with a maximum recorded concentration of up to 2030 ppm. The In concentration in the Zn ore zones locally reaches 3170 ppm. Element-element correlations (Fig. 8) based on geochemical assay results in diamond-drillholes from the Isabel deposit indicate that In has a strong positive correlation with Cu ($r = 0.7$), Sn ($r = 0.6$), and Zn ($r = 0.6$), and a weak positive correlation with Ag ($r = 0.4$; Fig. 8).

5. Results

5.1. *Petrography and mineral paragenesis*

A simplified mineral paragenesis sequence of the ore minerology is presented in Fig. 9 for the Baal Gammon and Isabel deposits. Chalcopyrite containing inclusions of sphalerite is the most abundant sulfide mineral at the Baal Gammon deposit, and is in association with pyrrhotite forming massive sulfides. The early cassiterite phase has altered to In-rich stannite in the massive sulfides (Fig. 10a-b). Element composition maps indicate that the stannite is rich in Zn, Sn, and In (Fig. 10c-e). At the Isabel deposit, sphalerite is the dominant sulfide and contains inclusions of chalcopyrite (Fig. 11a). The early cassiterite in the Type I veins were partially replaced by chalcopyrite, giving it a slightly porous texture (Fig. 7e and Fig. 11a). Complete cassiterite alteration was not observed in the Isabel deposit and only dissolution and replacement textures are present (Fig. 7e). Stannite was observed in the Type II veins at the Isabel deposit (Fig. 11b) along the boundary of sphalerite and galena, but mostly in sphalerite.

5.2. *Indium content of sphalerite, chalcopyrite and pyrrhotite*

The LA-ICP-MS analyses indicate that the main host for In is sphalerite and chalcopyrite. The In content of sphalerite from the Baal Gammon deposit varies between 3009 and 6795 ppm (Table 1), whereas the In content of sphalerite from the Isabel deposit varies between 1303 and 1565 ppm (Table 2). The Sn and Cu content of sphalerite from both deposits are highly variable (Fig. 12), indicating the presence of micro-inclusions of chalcopyrite and cassiterite-stannite. The In content of

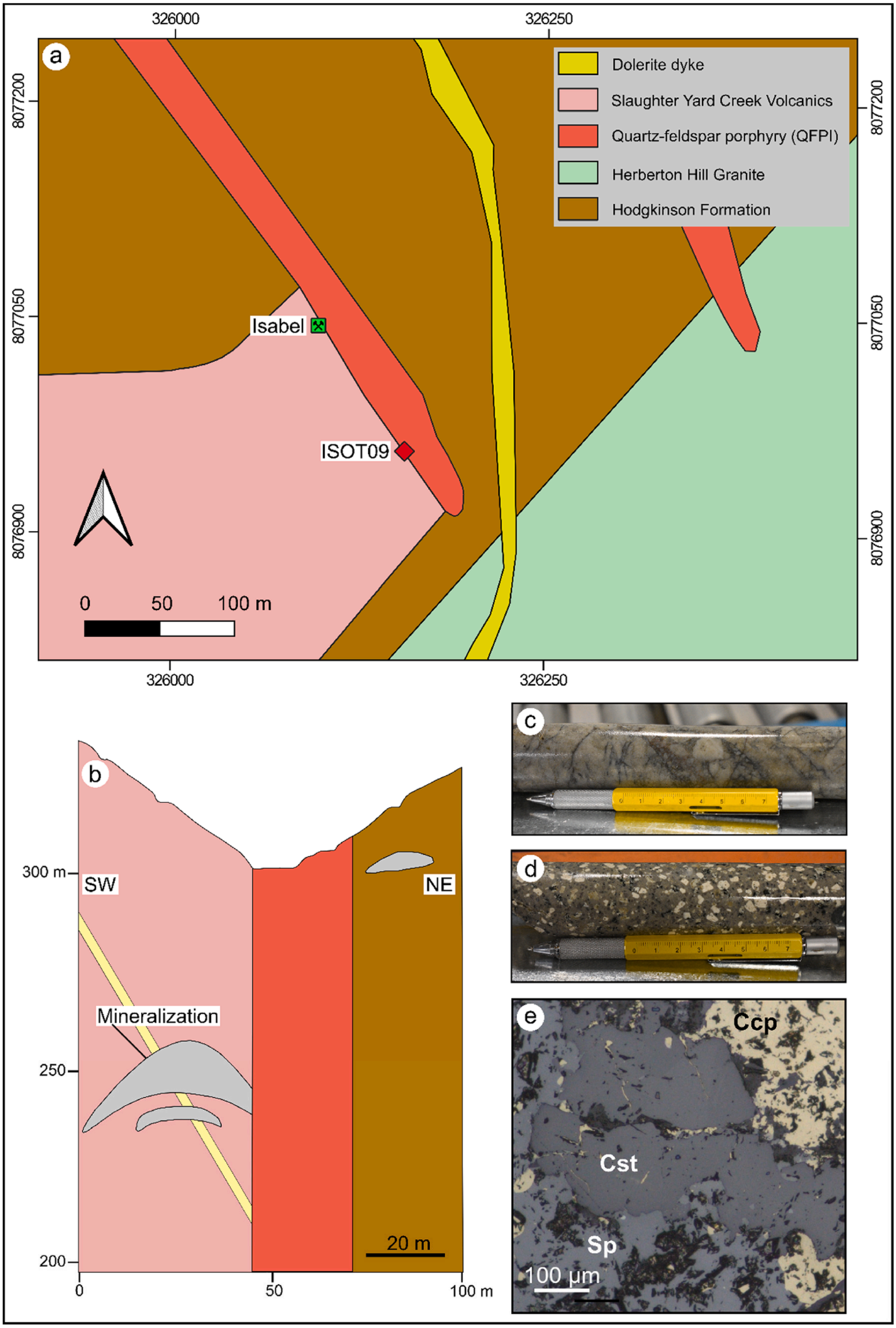

Fig. 7. Maps and photographs showing: (a) geological map of the Isabel area; (b) cross-section showing mineralization and crosscutting units at the deposit; (c) mineralized hydrothermal breccia; (d) unit QFPI; and (e) reflected light photomicrograph of cassiterite (Cst) in sphalerite (Sp) and chalcopyrite (Ccp) vein.

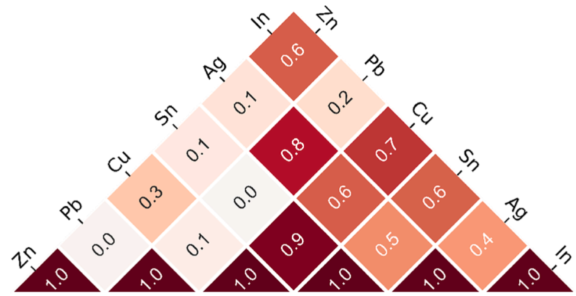

Fig. 8. Element-element correlation matrix for geochemical assay data from the Isabel diamond-drill core. Approximately 80 assays were taken for developing the correlation matrix from 10 diamond-drill holes and values above the detection limit were used.

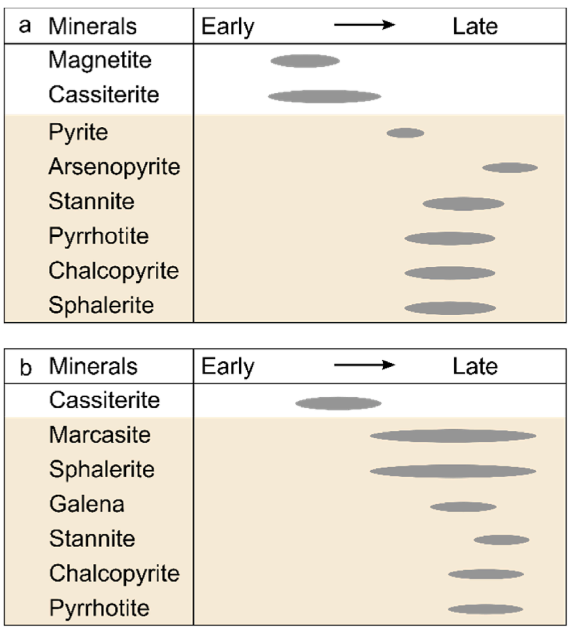

Fig. 9. A simplified paragenesis illustration of ore minerals at: (a) the Baal Gammon deposit; and (b) the Isabel deposit.

chalcopyrite from the Baal Gammon deposit varies between 1071 and 1727 ppm (Table 1), whereas the In content of chalcopyrite from the Isabel deposit varies between 573 and 857 ppm (Table 2). The Zn content of chalcopyrite from the Baal Gammon deposit varies between 727 and 1896 ppm, whereas the Sn content varies between 1323 and 2354 ppm (Table 1). For the Isabel deposit, the Zn and Sn content of chalcopyrite (Table 2; Fig. 12) is highly variable indicating the presence of several micro-inclusions of sphalerite and cassiterite-stannite. Pyrrhotite commonly does not incorporate large amounts of In, Sn and Zn in its crystal structure, and large variability observed in the concentration of these elements indicates the presence of several micro-inclusions (Fig. 12).

5.3. Zircon geochronology

5.3.1. The Baal Gammon deposit

Zircon grains extracted from sample BGOT009 from the UNA Porphyry at the northern part of the Baal Gammon pit have low luminescence, are elongated and euhedral with only few subhedral crystals (Figs. 2 and 13a). Fifty-seven spots on these zircons were analysed, yielding two distinct age populations. The younger population consists of 21 concordant analyses yielding a $^{206}Pb/^{238}U$ weighted mean age of 333 ± 2 Ma and an identical concordia age (Fig. 14a). The older population consists of 36 concordant analyses yielding a $^{206}Pb/^{238}U$ weighted mean age of 363 ± 1 Ma and an identical concordia age (Fig. 14a). The younger population is interpreted as the emplacement age for the UNA Porphyry whereas the older population is interpreted as zircons inheritance from the Jumna Granite.

Samples BG01, BG02 and BGW03 were collected from dykes mapped as the Slaughter Yard Creek Volcanics. Sample BG01 was collected from a quartz-feldspar porphyry dyke (QFP) from the western side of the deposit (Fig. 2). The zircon grains separated from this sample are elongated and euhedral with moderate luminescence and concentric zoning typical for magmatic zircons (Fig. 13b). Forty-seven concordant analyses yield a $^{206}Pb/^{238}U$ weighted mean age of 289 ± 1 Ma and an identical concordia age (Fig. 14b) interpreted as the emplacement age for the dyke. Sample BG02 was collected from a medium-grained porphyry dyke (MGPD) ~45 m NW of sample BG01. The zircon grains separated from this sample are similar in appearance to those from sample BG01. Forty-two concordant analyses yield a $^{206}Pb/^{238}U$ weighted mean age of 288 ± 1 Ma and an identical concordia age (Fig. 14c), which are interpreted as the emplacement age for this dyke. Sample BGW03 was collected from a shallow level intrusive rhyolite dyke that outcrops in the eastern part of the deposit (Fig. 2). The zircon grains separated from this sample are similar in appearance to those separated from samples BG01 and BG02 (Fig. 13). Thirty-four concordant analyses yield a $^{206}Pb/^{238}U$ weighted mean age of 288 ± 1 Ma and an identical concordia age interpreted as the emplacement age for the dyke (Fig. 14d).

5.3.2. Isabel deposit

A sample of brecciated meta-sandstone (ISOT04) from the Hodgkinson Formation that hosts polymetallic vein mineralization was collected from near the Isabel deposit. Some of the zircon grains extracted from this sample are brown, indicative of a high uranium content. The brown zircons have rounded edges, while most of the clear zircon grains appear euhedral and elongated. The zircon grains have variable luminescence and internal zoning. Two-hundred-eleven analyses were performed, and 161 analyses had a discordance of <10%. Individual $^{206}Pb/^{238}U$ ages range from 2989 ± 55 to 409 ± 9 Ma. Two populations can be identified on a kernel density estimate (KDE) plot (Fig. 14e). One population peaks at 1605 Ma and the other at 457 Ma. The younger age was interpreted as the maximum depositional age for the meta-sandstone sample.

Sample ISOT09 was collected from a quartz-porphyry dyke (QFPI) that intruded the meta-sandstone near the Isabel deposit (Fig. 7). The zircon grains separated from the sample are elongated and euhedral with concentric zoning and moderate luminescence (Fig. 13f). Forty-three analyses yielded concordant ages with a $^{206}Pb/^{238}U$ weighted mean of 292 ± 1 Ma and an identical concordia age (Fig. 14f), interpreted as the emplacement age for the dyke.

5.3.3. Regional granite units and volcanic rocks

Four samples (HBH01, JM05, WT03, and KG06) were collected from granites that intruded the Hodgkinson Formation near the Baal Gammon and Isabel deposits, and two samples (GGV01 and GGV02) were collected from the Slaughter Yard Creek Volcanics near the Isabel deposit (Fig. 1c). Sample HBH01 was collected from the Herberton Hill Granite near the Isabel deposit. The zircon grains separated from the sample are euhedral and elongated with concentric zoning and moderate luminescence. Eleven analyses yielded concordant ages with a $^{206}Pb/^{238}U$ weighted mean of 340 ± 3 Ma and an identical concordia age (Fig. 15a), interpreted as the emplacement age for the Herberton Hill Granite. Sample JM05 was collected from the Jumna Granite ~1.6 km SW of the Baal Gammon deposit (Fig. 1). The zircon grains separated from this sample are euhedral and elongated with concentric zoning and low luminescence. Nine analyses yielded concordant ages with a $^{206}Pb/^{238}U$ weighted mean age of 367 ± 2 Ma with an identical

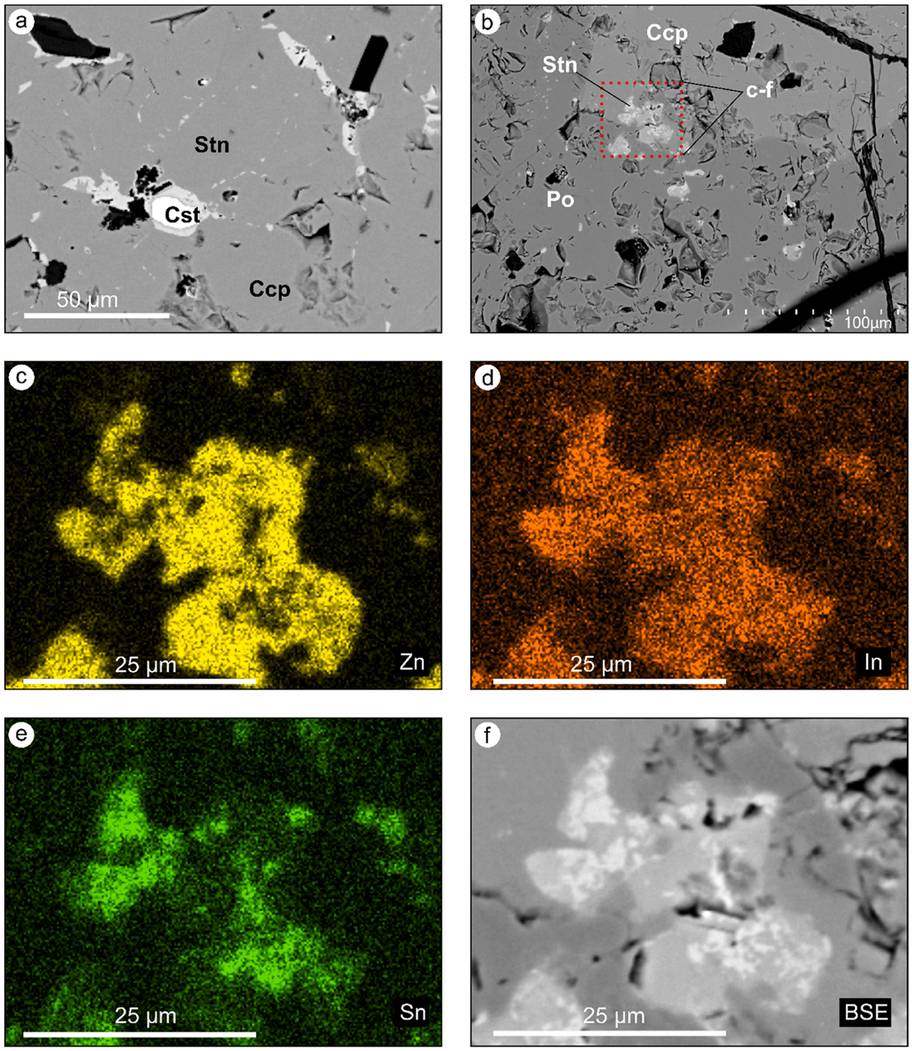

Fig. 10. Electron backscatter images and element maps of massive sulfide ore from the Baal Gammon deposit. (a) BSE image of cassiterite (Cst) altered to stannite (Stn) in chalcopyrite (Ccp); (b) BSE image of In-rich stannite occurring in chalcopyrite and pyrrhotite (Po) assemblage of massive sulfides; (c) element distribution map of Zn; (d) element distribution map of In; (e) element distribution map of Sn; and (f) BSE image of the mapped stannite grain.

concordia age (Fig. 15b), which has been interpreted as the emplacement age for the Jumna Granite. Sample WT03 was collected from the Watsonville Granite ~1.6 km north of the Baal Gammon deposit (Fig. 1). The zircon grains separated from this sample are like the ones separated from the Jumna Granite. Nineteen analyses yielded concordant ages with a $^{206}Pb/^{238}U$ weighted mean age of 283 ± 1 Ma and a slightly older concordia age of 285 ± 1 Ma (Fig. 15c). The $^{206}Pb/^{238}U$ weighted mean age of 283 ± 1 Ma is interpreted as the emplacement age of the Watsonville Granite. Sample KG06 was collected from the Kalunga Granodiorite ~1 km south of the Isabel deposit (Fig. 1). The zircon grains separated from this sample are elongated and euhedral with moderate luminescence and concentric zoning. Thirteen analyses yielded concordant ages with a $^{206}Pb/^{238}U$ weighted mean age of 314 ± 2 Ma and a similar concordia age of 316 ± 2 Ma (Fig. 15d). The former has been interpreted as the emplacement age for the Kalunga Granodiorite.

Sample GGV01 was collected from the Slaughter Yard Creek Volcanics ~600 m northwest of the Isabel deposit (Fig. 1). The zircon grains separated from the sample are elongated, euhedral with low luminescence, and most are not zoned. Twelve analyses yielded concordant ages with a $^{206}Pb/^{238}U$ weighted mean age of 292 ± 1 Ma and an identical concordia age (Fig. 15e), interpreted as the emplacement age. Sample GGV02 was collected from a flow-banded rhyolite in the Slaughter Yard Creek Volcanics (Fig. 1). Zircon grains separated from the sample are subhedral and have low luminescence with no visible zoning. Twenty analyses yielded concordant ages with a $^{206}Pb/^{238}U$ weighted mean age of 325 ± 1 Ma and an identical concordia age (Fig. 15f), interpreted as the emplacement age for this unit.

6. Discussion

6.1. Indium distribution in the Baal Gammon and Isabel deposits

The ore mineralogy (Figs. 3, 7, 10, and 11), SEM and LA-ICP-MS analysis of sulfides, together with multielement correlation matrixes (Figs. 6 and 8) can be used to make inferences about the distribution of In at the Baal Gammon and Isabel deposits. Cassiterite and chalcopyrite are the major ore minerals at the Baal Gammon deposit, and sphalerite and galena are the major ore minerals at the Isabel deposit. Cassiterite incorporates minor amounts of In (up to 304 ppm; Pavlova et al., 2015), and it is unlikely to be a major host for In at either of the deposits. The SEM results indicate that cassiterite has altered to stannite (Fig. 10) and incorporated In content >0.5 wt%. Stannite was observed in the massive sulfides of the Baal Gammon deposit and Type II veins at the Isabel deposit.

Chalcopyrite can incorporate up to 4000 ppm In (Sinclair et al., 2006). The strong correlation between In and Cu observed at Baal

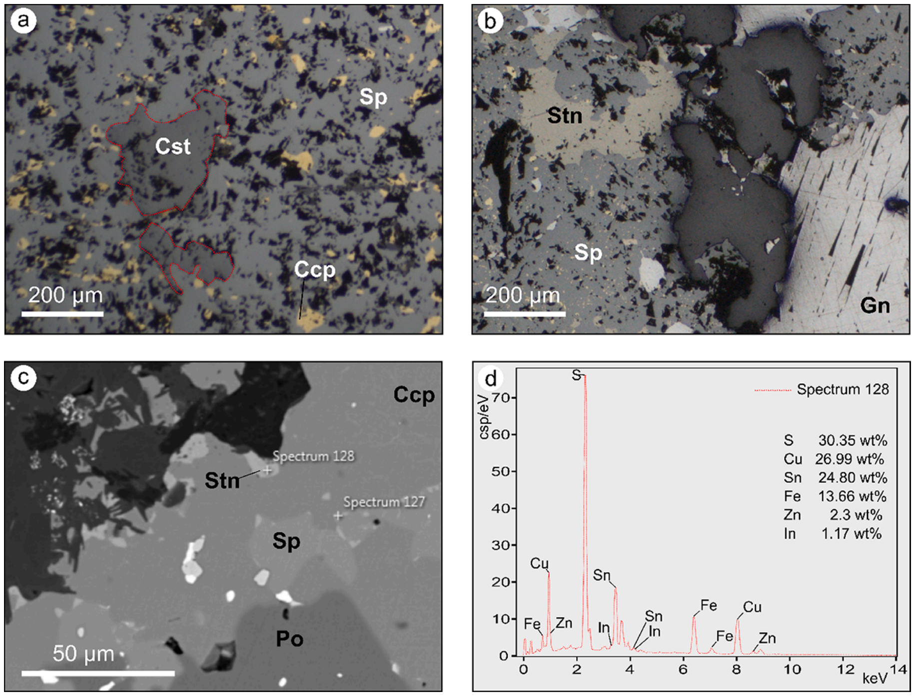

Fig. 11. Microphotographs (a-b) and electron backscatter image (c) of ore from the Isabel deposit: (a) Type I vein of sphalerite (Sp) with chalcopyrite (Ccp) inclusion and cassiterite (Cst); (b) Type II vein of sphalerite and galena (Gn) with In-bearing stannite (Stn); (c) BSE image showing the distribution of stannite in a cross-cutting vein of chalcopyrite and pyrrhotite; and (d) energy dispersive X-ray spectra showing the identification of stannite phase at spot labelled as Spectrum 128 in Fig. 11c.

Gammon implies that chalcopyrite hosts a significant amount of In (Fig. 6; r = 0.9). In situ LA-ICP-MS analysis of chalcopyrite indicates a mean In content of 1244 ppm (Table. 1).

Sphalerite can incorporate >6 wt% In (Bauer et al., 2019; Murakami and Ishihara, 2013; Torró et al., 2019; Valkama et al., 2016), through a coupled substitution of In^{3+} and Cu^{+} for two Zn^{2+} atoms (e.g. Bauer et al., 2019; Cook et al., 2012; Shaw, 1952; Xu et al.,2021). Additionally, Ag^{+}, Sn^{3+}, and Sb^{3+} can be involved in this substitution (Belissont et al., 2014; Schirmer et al., 2020). Even though higher In content averaging 4042 ppm was measured in sphalerite from the Baal Gammon deposit (Table 1), the moderate correlation between In and Zn (r = 0.4) and the lower density of inclusion in the massive sulfides suggests that sphalerite contributes less than chalcopyrite to the overall In budget. At the Isabel deposit, In displays moderate correlations (Fig. 8) with Zn (r = 0.6), Sn (r = 0.6) and Cu (r = 0.7). These three elements (Zn, Sn and Cu) are the primary constituents of stannite. In addition, the correlations, SEM (Fig. 11), and LA-ICP-MS analysis (Table 2; Fig. 12) indicate that chalcopyrite, sphalerite, and stannite are the major hosts for In in the Isabel deposit.

6.2. *Timing of mineralization*

The timing of mineralization at the Baal Gammon and Isabel deposits is constrained based on field relationships, and zircon geochronology. The oldest phase of the mineralization comprises disseminated cassiterite hosted by the UNA Porphyry at Baal Gammon, and disseminated cassiterite in polymetallic veins at Isabel. The 333 ± 2 Ma (Fig. 14a) emplacement age for the UNA Porphyry constrains the maximum age for tin mineralization at Baal Gammon. The timing of tin mineralization at Isabel is constrained by Sn-bearing granites associated with the deposit.

As discussed earlier, the Isabel deposit is located near the contact between the Hodgkinson Formation and the Herberton Hill Granite (Fig. 7a). Similar vein-hosted cassiterite mineralization is present throughout the Herberton Hill Granite and the Hodgkinson Formation (Fig. 1b-c; Robinson, 1983), suggesting that the mineralization hosted by the granite and host rocks are related. The Herberton Hill Granite is a composite intrusive body, which yields emplacement ages of between 339 ± 2 and 322 ± 4 Ma (Fig. 15a; Murgulov et al., 2013). Tin mineralization is present in all phases of the Herberton Hill Granite, which indicates that the maximum age for tin mineralization can be constrained by the youngest phase of the granite at 322 ± 4 Ma. This age is identical to the $^{206}Pb/^{238}U$ cassiterite age of 318 ± 2 Ma within error obtained from the same supersuite to represent the overall timing of tin mineralization in the HMF (Cheng et al., 2018; 2019).

The cassiterite mineralization is overprinted by stannite at the Baal Gammon and Isabel deposits (Figs. 3 and 7). This indicates that the sulfide mineralization is younger than ca. 318 Ma. Direct relationships between crosscutting dykes and sulfide mineralization at the Baal Gammon and Isabel deposits can be used to constrain the minimum age of mineralization (Fig. 3c and Fig. 7a-b). The QFP dyke that crosscuts the mineralization at the Baal Gammon deposit dates at 289 ± 1 Ma, and the crosscutting dyke (QFPI) at the Isabel deposit returned a similar age of 292 ± 1 Ma (Fig. 14b, f). Thus, the timing of the sulfide mineralization can be constrained between the age of the tin mineralization (ca. 318 Ma) and the age of crosscutting dykes (ca. 290 Ma). The close spatial and temporal relationship between the ca. 290 Ma porphyry dykes and the sulfide mineralization at Baal Gammon and Isabel suggest the possibility of a genetic connection. The presence of vermicular quartz and embayment textures in quartz phenocrysts from these dykes indicate a magmatic to hydrothermal transition. Porphyry dykes that display similar textures at the Empire Mine, Idaho, USA, have been linked to mineralization processes (Chang and Meinert, 2004).

6.3. *Significance of the new age data and the tectonic setting of the Herberton Mineral Field*

The age data presented in this study indicate that magmatic events dated between ca. 365 and 280 Ma have affected the HMF (Table. 3; Figs. 10 and 11), which overlaps with the igneous activity related to the Kennedy Igneous Association (Fig. 16a). The U-Pb zircon ages obtained in this study, in combination with the geochronological data from Cheng et al. (2017), indicate four pulses of magmatic activity peaked at ca. 337,

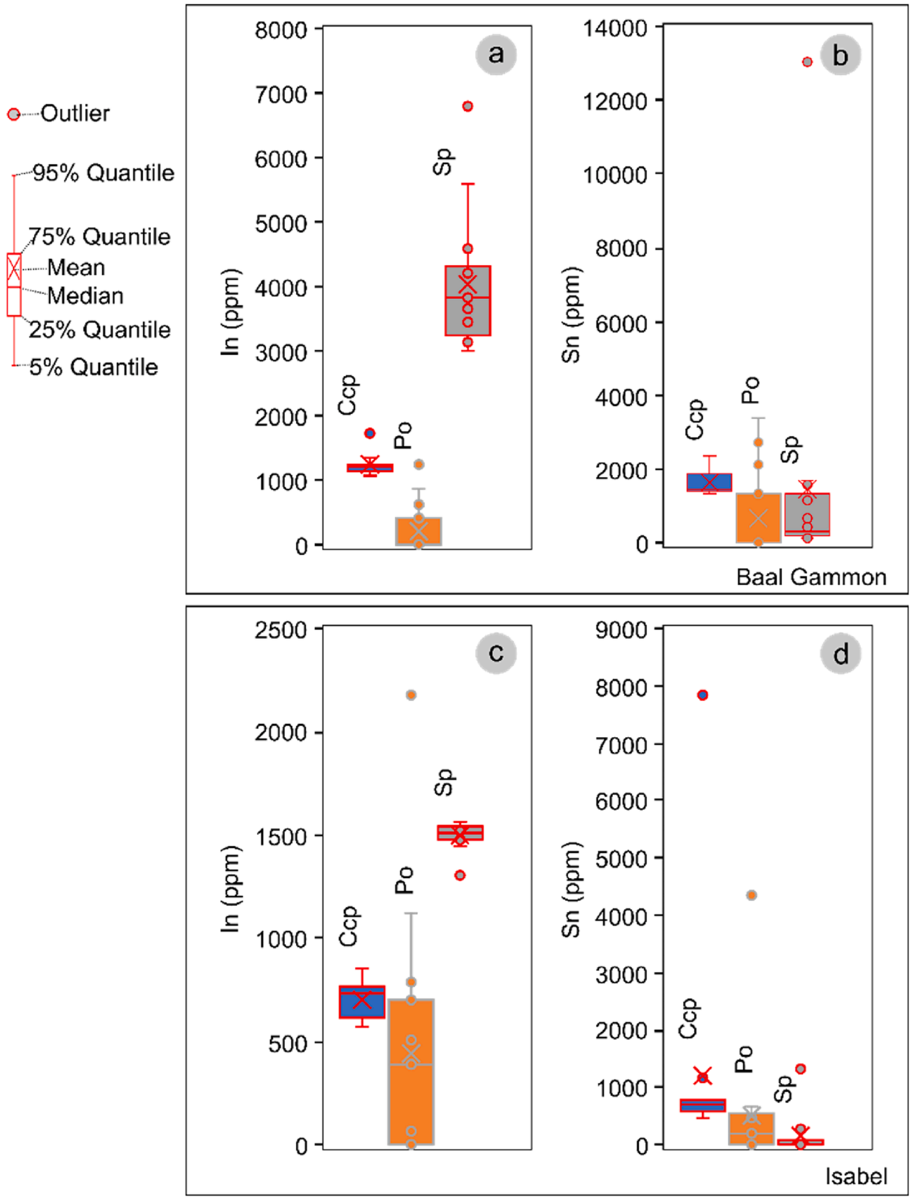

Fig. 12. Indium and Sn content of chalcopyrite (Ccp), pyrrhotite (Po), and sphalerite (Sp) from: (a-b) the Baal Gammon deposit; and (c-d) the Isabel deposit.

322, 305, and 285 Ma (Fig. 16a). The ca. 365 Ma age of the Jumna Granite is 25 Myrs older than the earliest intrusions recognized as part of the Kennedy Igneous Association (ca. 340–275 Ma; Champion and Bultitude, 2013a). Further east, the Mount Formartine Granite, which also intrudes the Hodgkinson Formation, is dated at 376 ± 3 Ma (Cross et al., 2019; Kositcin et al., 2015). It is unclear if this age indicates an earlier onset of magmatism associated with the Kennedy Igneous Association, or if it represents a late-stage magmatic activity related to the Tabberabberan Orogeny.

Two major detrital zircon populations were identified in the Hodgkinson Formation with peaks at ca. 1605 and 457 Ma, which indicate a likely provenance of these sedimentary rocks from the Thomson Orogen and Georgetown Inlier. These provinces were most likely situated to the west and south of the Mossman Orogen at the time of deposition of the Hodgkinson Formation (Henderson et al., 2013). Although, it was proposed that a small portion of the Thomson Orogen (e.g. the Barnard Province) bounds the Mossman Orogen to the east (Dirks et al., 2021), it is unlikely that these sedimentary rocks were sourced from the east as there are no known Proterozoic rocks east of the Tasman Line (Fig. 1). A younger detrital age of ca. 370 Ma reported by Kositcin and Bultitude (2015) from different parts of the Hodgkinson Formation may suggest diachronous sedimentation or multiple sediment sources.

The four magmatic events identified in this study are broadly coeval with those defined by Cheng et al. (2018) and are typically observed in the Kennedy Igneous Association of northeast Queensland (Champion and Bultitude, 2013a). The Hf and Nd isotope data from the Kennedy Igneous Association are indicative of a progressively more juvenile source that was involved in the generation of these magmas, which signifies a transition from crustal-derived melts to increased mantle input between 337 and 285 Ma (Champion and Bultitude, 2013b; Cheng et al., 2018). Accordingly, we agree with the model proposed by Cheng et al. (2018) and suggest that the tectonic setting of the magmatic activity during ca. 337 and 322 Ma compressional, whereas the magmatic activity at ca. 305 and 285 Ma was during a period of crustal thinning with an increased mantle input (Fig. 16b). The voluminous granitoids that formed during these crustal thickening and thinning episodes of the Kennedy Igneous Association were likely formed in a back-arc setting and the overall north–south trend of magmatism (Fig. 1a) was interpreted to indicate a west dipping subduction margin along the east coast of Australia (e.g. Vos et al., 2007; Withnall and Henderson, 2012).

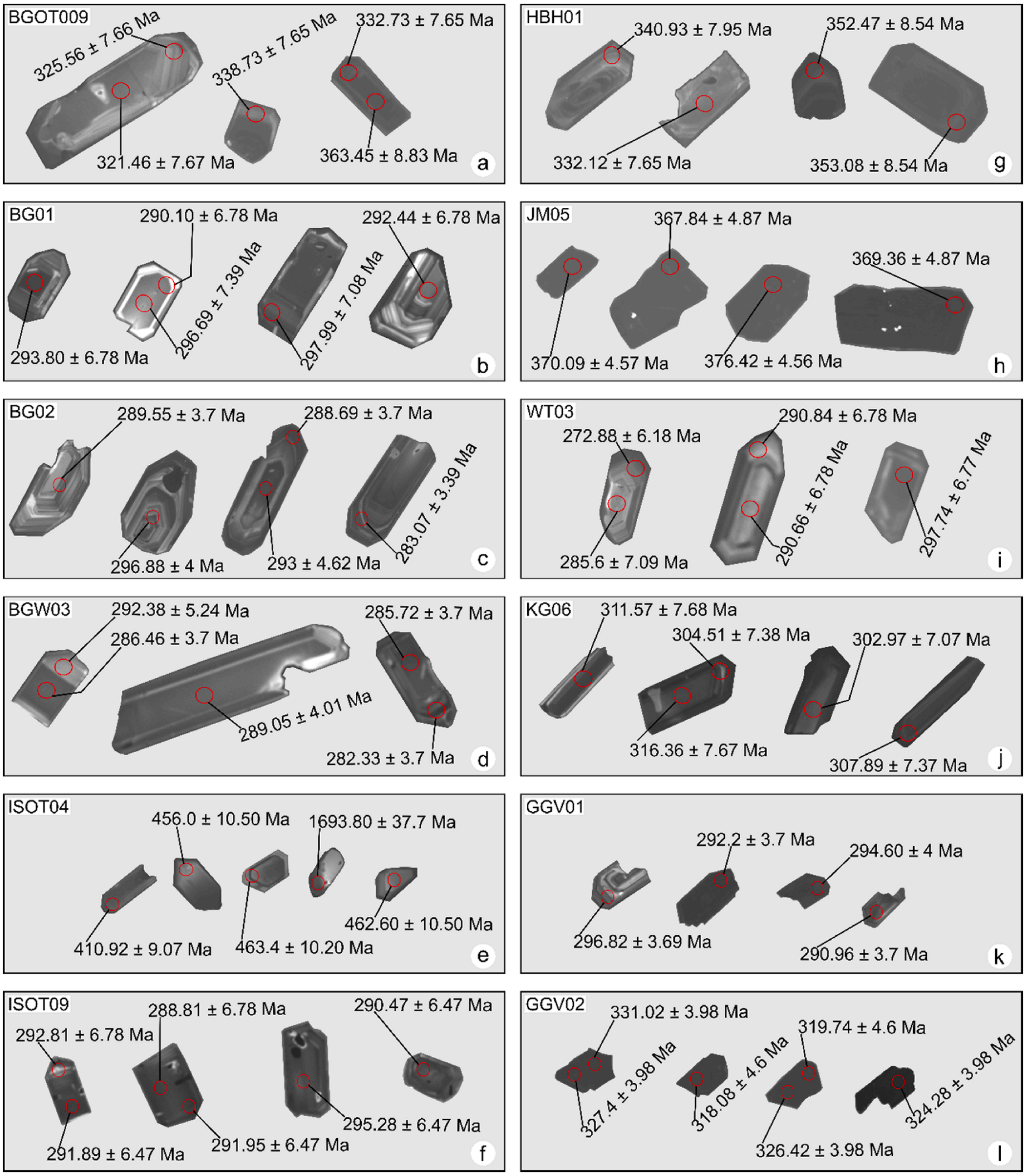

Fig. 13. Cathodoluminescence images of zircon grains from the Baal Gammon and Isabel deposits, and the Herberton Mineral Field.

Furthermore, these granitoids have a younging direction from south towards northeast (Cheng et al., 2017), suggesting a northerly migration of the magmatic activity along the subduction system. The switch from evolved, crust-derived magmas to juvenile magmas with higher mantle input interpreted by Cheng et al. (2018) as a transition from Sn dominated to W-Mo dominated mineralization. Our data suggest that sulfide mineralization and the associated enrichment of In postdated the Sn mineralization, and the sulfides were most likely related to the emplacement of the porphyry dykes at ca. 290 Ma. If that is the case, the In mineralization took place during a period of crustal thinning and was caused by juvenile magmas with a greater mantle input.

7. Conclusion

The Baal Gammon and Isabel deposits are the only deposits in the HMF with defined In resources. Tin mineralization, however, is overprinted by sulfides, as displayed in the two deposits, which is common throughout the HMF and linked to high-grade In mineralization. Indium mineralization appears to be predominantly hosted by the sulfide minerals chalcopyrite, sphalerite, and stannite. The timing of tin mineralization can be related to magmatic activity at ca. 320 Ma, whereas the sulfide mineralization is most likely related to the emplacement of porphyry dykes at ca. 290 Ma. The geodynamic setting of the HMF indicates deposition of tin mineralization in a compressional tectonic regime, while the sulfide and In were deposited during a period of crustal extension.

Declaration of Competing Interest

The authors declare that they have no known competing financial interests or personal relationships that could have appeared to influence the work reported in this paper.

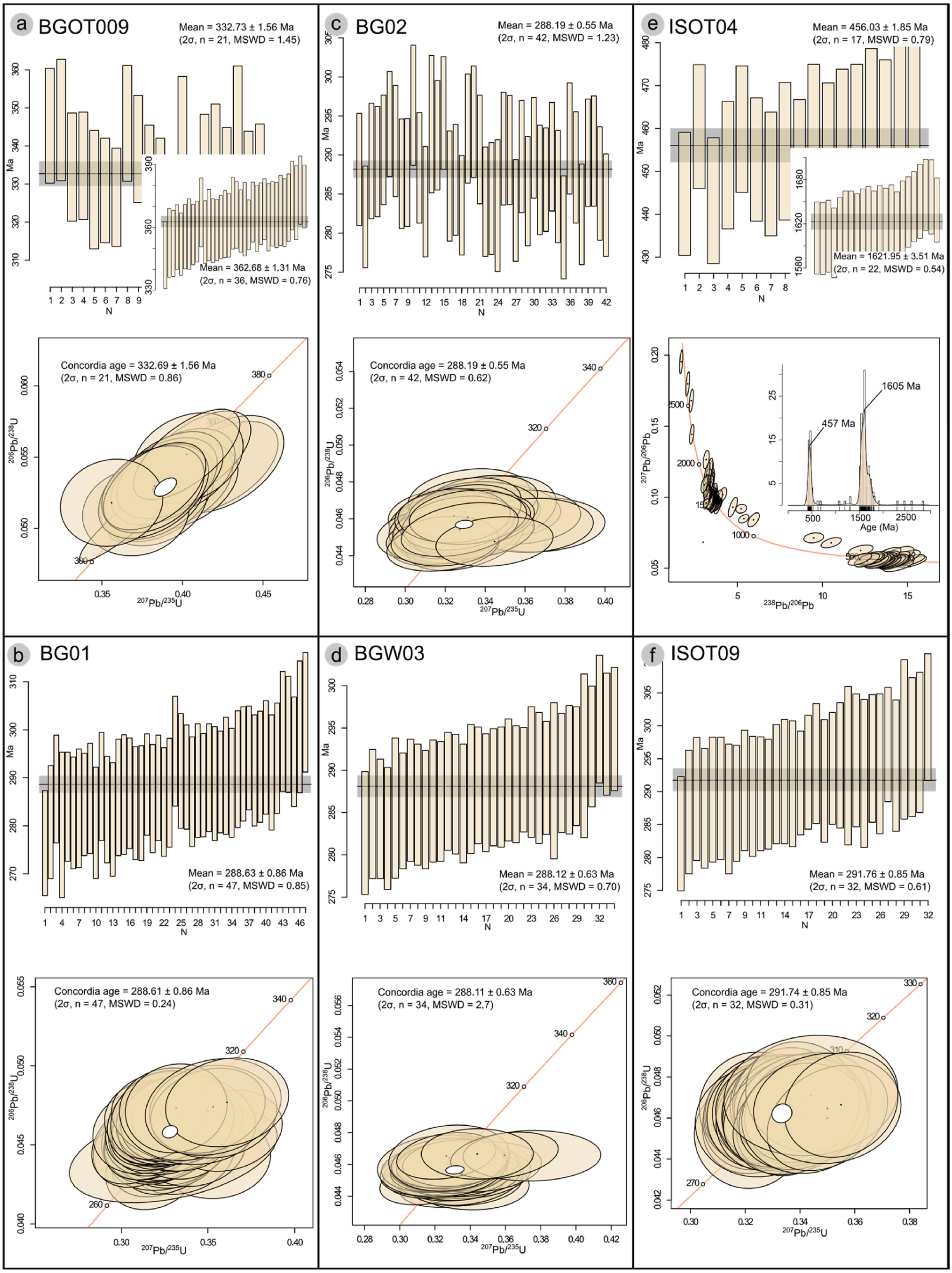

Fig. 14. $^{206}Pb/^{238}U$ weighted mean age (top) and concordia plot (bottom) for samples from Baal Gammon (a-d), and Isabel (e-f). The KDE plot is shown for sample ISOT04.

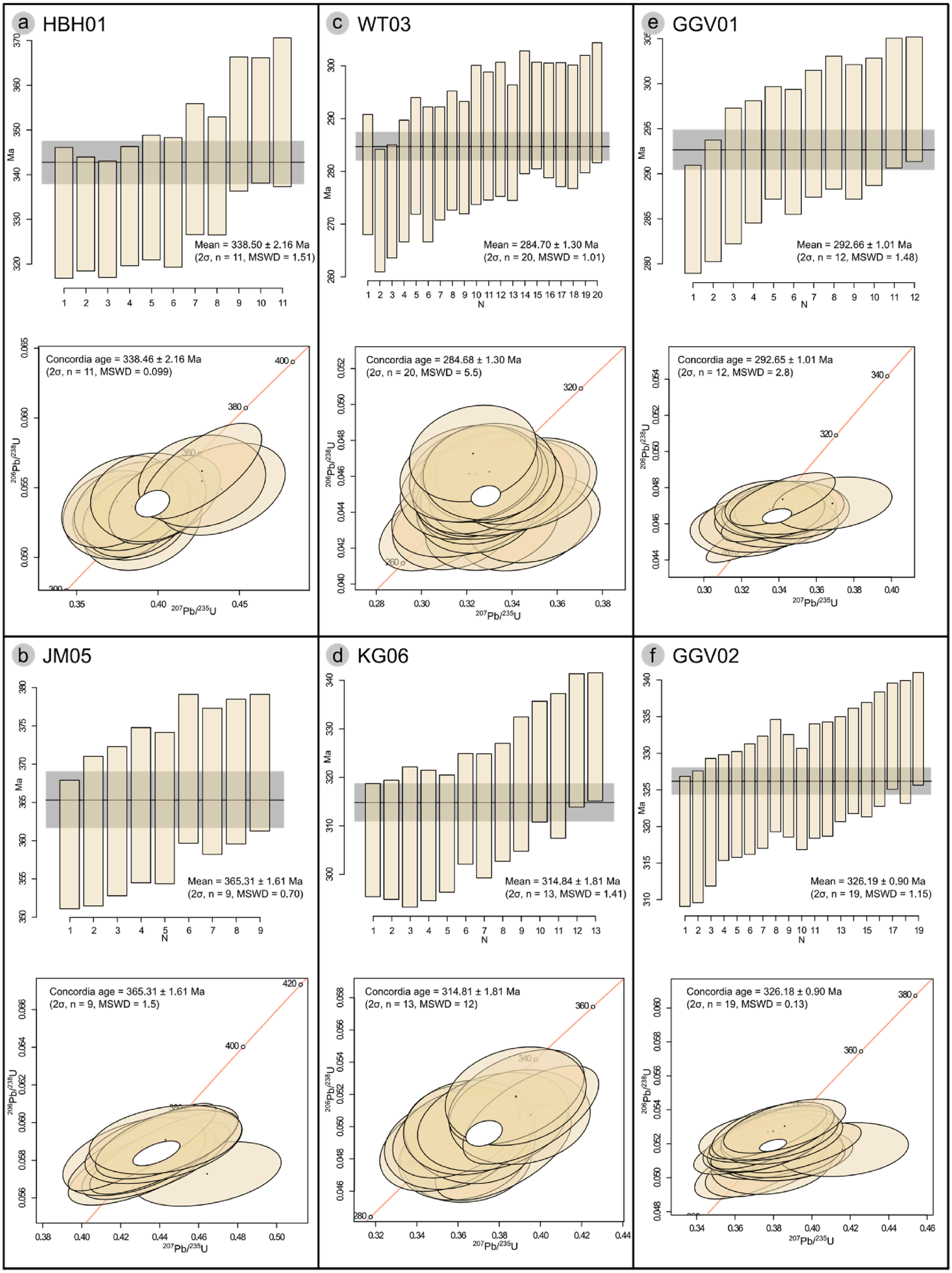

Fig. 15. $^{206}Pb/^{238}U$ weighted mean age (top) and concordia plots (bottom) for samples: (a) WT03; (b) KG06; (c) HBH01; (d) JM05; (e) GGV01; and (f) GGV02.

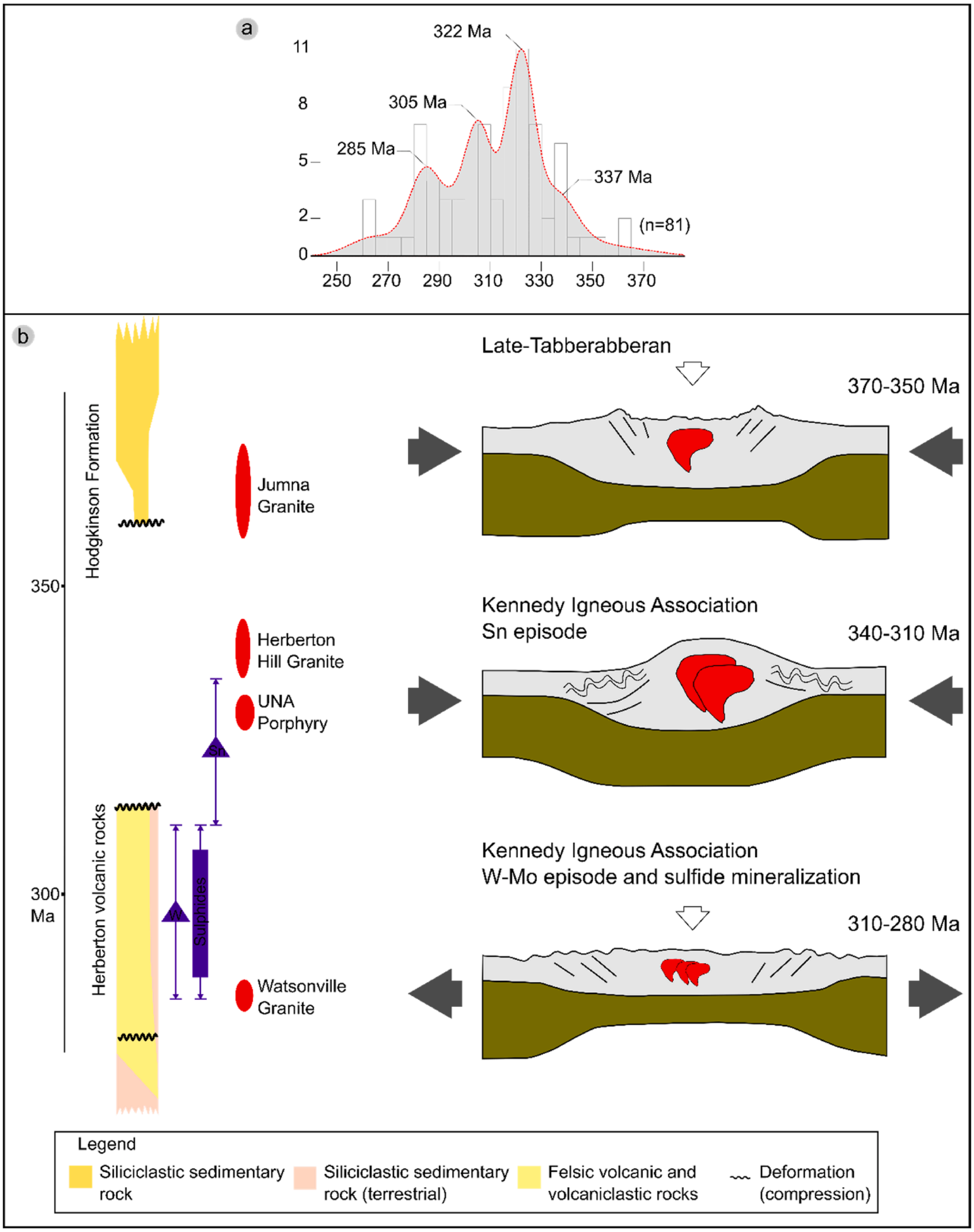

Fig. 16. Age distribution of felsic rocks from: (a) the Kennedy Igneous Association and an illustration of granite emplacement in the Herberton Mineral Field highlighting Sn, W, Mo, and sulfide mineralization; and (b) the stratigraphy (modified after Champion, 2016). The data for the age distribution plot is from Cheng et al. (2017) in combination with data from this study.

Data availability

Datasets related to this article can be found at https://doi.org/10.25903/09v7-r187, an integrated data management platform hosted at Research Data JCU (Kumar and Sanislav, 2022).

Acknowledgments

The Geological Survey of Queensland supported this study as part of the New Economy Minerals Initiative. AAK was supported by a Commonwealth Research scholarship at James Cook University. We thank the Economic Geology Research Centre (EGRU) at James Cook University (Townsville), Red River Resources Ltd., and Assoc. Prof. Paul Gow from Sustainable Minerals Institute (SMI) at The University of Queensland (Brisbane) for supporting us in conducting this research.

References

Bain, J.H.C., Draper, J.J., 1997. North Queensland Geology. Geological Survey of Queensland.

Bauer, M.E., Seifert, T., Burisch, M., Krause, J., Richter, N., Gutzmer, J., 2019. Indium-bearing sulfides from the Hämmerlein skarn deposit, Erzgebirge, Germany: evidence for late-stage diffusion of indium into sphalerite. Miner. Depos. 54, 175–192. https://doi.org/10.1007/s00126-017-0773-1.

Belissont, R., Boiron, M.-C., Luais, B., Cathelineau, M., 2014. LA-ICP-MS analyses of minor and trace elements and bulk Ge isotopes in zoned Ge-rich sphalerites from the Noailhac – Saint-Salvy deposit (France): Insights into incorporation mechanisms and ore deposition processes. Geochim. Cosmochim. Acta. 126, 518–540. https://doi.org/10.1016/j.gca.2013.10.052.

Blake, D.H., 1972. Regional and economic geology of the Herberton/Mount Garnet area-Herberton Tinfield, north Queensland. Geoscience Australia.

Carr, P.A., Zink, S., Bennett, V.C., Norman, M.D., Amelin, Y., Blevin, P.L., 2020. A new method for U-Pb geochronology of cassiterite by ID-TIMS applied to the Mole Granite polymetallic system, eastern Australia. Chem. Geol. 539, 119539 https://doi.org/10.1016/j.chemgeo.2020.119539.

Champion, D.C., 1991. The felsic granites of far north Queensland. The Australian National University, pp. 90–234. Unpubl. PhD thesis.

Champion, D.C., Bultitude, R.J., 2013a. Kennedy Igneous Association, in: Jell, P.A. (Ed.), Geology of Queensland. Geological Survey of Queensland, pp. 473–514.

Champion, D.C., Bultitude, R.J., 2013b. The geochemical and Sr-Nd isotopic characteristics of Paleozoic fractionated S-types granites of north Queensland: implications for S-type granite petrogenesis. Lithos 162–163, 37–56. https://doi.org/10.1016/j.lithos.2012.11.022.

Champion, D.C., 2016. Geodynamic Synthesis of the Phanerozoic of eastern Australia. Second edition. Geoscience Australia Record 2016/07. 10.11636/Record.2016.007.

Chang, Z., Meinert, L.D., 2004. The magmatic–hydrothermal transition—evidence from quartz phenocryst textures and endoskarn abundance in Cu–Zn skarns at the Empire Mine, Idaho, USA. Chem. Geol. 210, 149–171. https://doi.org/10.1016/j.chemgeo.2004.06.018.

Cheng, Y., Chang, Z., Clarke, G., Illig, P., Poblete, J., Liu, K., Johnson, R., Hall, C.M., Creaser, R.A., 2017. Geology and magmatic-hydrothermal temporal sequence of Sn-W-Mo-Au metallogeny in Northern Queensland. Unpublished report, Geological Survey of Queensland, Australia.

Cheng, Y., Spandler, C., Chang, Z., Clarke, G., 2018. Volcanic–plutonic connections and metal fertility of highly evolved magma systems: a case study from the Herberton Sn–W–Mo Mineral Field, Queensland, Australia. Earth Planet. Sci. Lett. 486, 84–93. https://doi.org/10.1016/j.epsl.2018.01.012.

Cheng, Y., Spandler, C., Kemp, A., Mao, J., Rusk, B., Hu, Y., Blake, K., 2019. Controls on cassiterite (SnO_2) crystallization: evidence from cathodoluminescence, trace-element chemistry, and geochronology at the Gejiu Tin District. Am. Mineral. 104, 118–129. https://doi.org/10.2138/am-2019-6466.

Clarke, G.W., Chang, Z., 2017. Magma-related hydrothermal mineral systems of the Northern Bowen Basin. Unpublished report, Geological Survey of Queensland.

Collins, P.L.F., Williams, E., 1986. Metallogeny and tectonic development of the Tasman Fold Belt system in Tasmania. Ore Geol. Rev. 1, 153–201. https://doi.org/10.1016/0169-1368(86)90008-9.

Cook, N.J., Ciobanu, C.L., Brugger, J., Etschmann, B., Howard, D.L., De Jonge, M.D., Ryan, C., Paterson, D., 2012. Determination of the oxidation state of Cu in substituted Cu-In-Fe-bearing sphalerite via μ-XANES spectroscopy. Am. Mineral. 97, 476–479. https://doi.org/10.2138/am.2012.4042.

Cross, A.J., Dhnaram, C., Lisitsin, V., Bultitude, R.J., Brown, D.D., Purdy, D.J., Von Gnielinski, F.E., 2019. Summary of results. Joint GSQ–GA geochronology project: Cairns, Cape York and Georgetown regions, 2015–2016. Geological Survey of Queensland.

Dash, P.H., Barker, R.M., Morwood, D.A., Culpeper, L.G., Lam, J.S.F., 1991. Mineral Occurrences-Atherton 1: 100 000 Sheet Area. Queensland Department of Resource Industries.

Denholm, J.L., Stepanov, A.S., Meffre, S., Bottrill, R.S., Thompson, J.M., 2021. The geochronology of tasmanian tin deposits using LA-ICP-MS U-Pb Cassiterite dating. Econ. Geol. 116, 1387–1407. https://doi.org/10.5382/econgeo.4837.

Dirks, H.N., Sanislav, I.V., Abu Sharib, A.S.A.A., 2021. Continuous convergence along the paleo-Pacific margin of Australia during the Early Paleozoic: Insights from the Running River Metamorphics, NE Queensland. Lithos 398–399, 106343. https://doi.org/10.1016/j.lithos.2021.106343.

Donchak, P.J.T., Bultitude, R.J., 1998. Explanatory Notes to accompany Atherton 1: 250 000 Geological Map, sheet SE 55-5. Geological Survey of Queensland.

Edgar, A., Sanislav, I.V., Dirks, P.H.G.M., 2022a. Tectonic setting and mineralisation potential of the Cowley Ophiolite Complex, north Queensland. Aust. J. Earth Sci. https://doi.org/10.1080/08120099.2022.2086173.

Edgar, A., Sanislav, I. v., Dirks, P.H.G.M., Spandler, C., 2022b. Metamorphic diamond from the northeastern margin of Gondwana: Paradigm shifting implications for one of Earth's largest orogens. Sci. Adv. 8, 2811. https://doi.org/10.1126/sciadv.abo2811.

Fergusson, C.L., Henderson, R.A., Blake, P.R., Bultidude, R.J., Champion, D.C., Cross, A. J., Draper, J.J., Green, T.J., Hutton, L.J., Jell, P.A., 2013. Thomson orogen, in: Jell, P.A. (Ed.), Geology of Queensland. Geological Survey of Queensland, pp. 113–221.

Fergusson, C.L., Henderson, R.A., Withnall, I.W., Fanning, C.M., 2007. Structural history of the Greenvale Province, north Queensland: Early Palaeozoic extension and convergence on the Pacific margin of Gondwana. Aust. J. Earth Sci. 54, 573–595. https://doi.org/10.1080/08120090701188970.

Fisher, C.M., Paton, C., Pearson, D.G., Sarkar, C., Luo, Y., Tersmette, D.B., Chacko, T., 2017. Data reduction of Laser Ablation Split-Stream (LASS) analyses using newly developed features within iolite: with applications to Lu-Hf + U-Pb in Detrital Zircon and Sm-Nd +U-Pb in Igneous Monazite. Geochem. Geophys. Geosyst. 18, 4604–4622. https://doi.org/10.1002/2017GC007187.

Fontana, D., Forte, F., Pietrantonio, M., Pucciarmati, S., 2021. Recent developments on recycling end-of-life flat panel displays: a comprehensive review focused on indium. Crit. Rev. Environ. Sci. Technol. 51, 429–456. https://doi.org/10.1080/10643389.2020.1729073.

Fraser, N., 1972. Geology and mineralization, United North Australian Mine, Watsonville, North Queensland. James Cook University. Unpubl. B.Sc. thesis.

Glen, R.A., 2005. The Tasmanides of eastern Australia. Geol. Soc. London Spec. Publ. 246, 23–96. https://doi.org/10.1144/GSL.SP.2005.246.01.02.

Glen, R.A., 2013. Refining accretionary orogen models for the Tasmanides of eastern Australia. Aust. J. Earth Sci. 60, 315–370. https://doi.org/10.1080/08120099.2013.772537.

Henderson, R.A., Donchak, P.J.T., Withnall, I.W., 2013. Mossman Orogen, in: Jell, P.A. (Ed.), Geology of Queensland. Geological Survey of Queensland, pp. 225–304.

Horstwood, M.S.A., Košler, J., Gehrels, G., Jackson, S.E., McLean, N.M., Paton, C., Pearson, N.J., Sircombe, K., Sylvester, P., Vermeesch, P., Bowring, J.F., Condon, D.J., Schoene, B., 2016. Community-derived standards for LA-ICP-MS U-(Th-)Pb Geochronology – Uncertainty propagation, age interpretation and data reporting. Geostand. Geoanalytical Res. 40, 311–332. https://doi.org/10.1111/j.1751-908X.2016.00379.x.

Jackson, S.E., Pearson, N.J., Griffin, W.L., Belousova, E.A., 2004. The application of laser ablation-inductively coupled plasma-mass spectrometry to in situ U-Pb zircon geochronology. Chem. Geol. 211, 47–69. https://doi.org/10.1016/j.chemgeo.2004.06.017.

Johnston, C., Black, L.P., 1986. Rb-Sr systematics of the Coolgarra Batholith, North Queensland. Aust. J. Earth Sci. 33, 309–324. https://doi.org/10.1080/08120098608729368.

Korges, M., Weis, P., Lüders, V., Laurent, O., 2020. Sequential evolution of Sn–Zn–In mineralization at the skarn-hosted Hämmerlein deposit, Erzgebirge, Germany, from fluid inclusions in ore and gangue minerals. Miner. Depos. 55, 937–952. https://doi.org/10.1007/s00126-019-00905-4.

Kositcin, N., Bultitude, R.J., 2015. Summary of Results-Joint GSQ-GA Geochronology Project: Hodgkinson Formation of the Mossman Orogen, 2014-2015. Geological Survey of Queensland.

Kositcin, N., Bultitude, R.J., Purdy, D.J., Brown, D.D., Carr, P.A., Lisitsin, V., 2015. Summary of Results-Joint GSQ-GA Geochronology Project: Kennedy Igneous Association, Mossman Orogen, Thomson Orogen and Iron Range Province: Kennedy Igneous Association, Mossman Orogen, Thomson Orogen and Iron Range Province, 2013-2014. Geological Survey of Queensland.

Kositcin, N., Huston, D.L., Champion, D.C., 2009. Geodynamic synthesis of the north Queensland region and implications for metallogeny. Geoscience Australia.

Kumar, A., Sanislav, I., 2022. Zircon U-Pb ages for the Herberton Mineral Field. James Cook University. https://doi.org/10.25903/09v7-r187.

Mackenzie, D.E., 1993. Geology of the Featherbed Cauldron Complex, north Queensland: Part 1-eruptive rocks and post-volcanic sediments. Australian Geological Survey Organisation.

Murakami, H., Ishihara, S., 2013. Trace elements of Indium-bearing sphalerite from tin-polymetallic deposits in Bolivia, China and Japan: a femto-second LA-ICPMS study. Ore Geol. Rev. 53, 223–243. https://doi.org/10.1016/j.oregeorev.2013.01.010.

Murgulov, V., Beyer, E., Griffin, W.L., O'Reilly, S.Y., Walters, S.G., Stephens, D., 2007. Crustal evolution in the Georgetown Inlier, North Queensland, Australia: a detrital zircon grain study. Chem. Geol. 245, 198–218. https://doi.org/10.1016/j.chemgeo.2007.08.001.

Murgulov, V., Griffin, W.L., O'Reilly, S.Y., 2013. Carboniferous and Permian granites of the northern Tasman orogenic belt, Queensland, Australia: insights into petrogenesis and crustal evolution from an in situ zircon study. Int. J. Earth Sci. 102, 647–669. https://doi.org/10.1007/s00531-012-0837-5.

Paton, C., Hellstrom, J., Paul, B., Woodhead, J., Hergt, J., 2011. Iolite: Freeware for the visualisation and processing of mass spectrometric data. J. Anal. At. Spectrom. 26, 2508. https://doi.org/10.1039/c1ja10172b.

Pavlova, G.G., Palessky, S.V., Borisenko, A.S., Vladimirov, A.G., Seifert, T., Phan, L.A., 2015. Indium in cassiterite and ores of tin deposits. Ore Geol. Rev. 66, 99–113. https://doi.org/10.1016/j.oregeorev.2014.10.009.

Pollard, P.J., 1988. Petrogenesis of tin-bearing granites of the Emuford district, Herberton tinfield, Australia. Aust. J. Earth Sci. 35, 39–57. https://doi.org/10.1080/08120098808729438.

Ren, S.K., Walshe, J.L., Paterson, R.G., Both, R.A., Andrew, A., 1995. Magmatic and hydrothermal history of the porphyry-style deposits of the Ardlethan tin field, New South Wales, Australia. Econ. Geol. 90, 1620–1645. https://doi.org/10.2113/gsecongeo.90.6.1620.

Robinson, C.C., 1983. The geology and mineralisation of the Isabel Mine, Herberton, Queensland. James Cook University. Unpubl. M.Sc. thesis.

Rosenbaum, G., 2018. The Tasmanides: phanerozoic tectonic evolution of Eastern Australia. Annu. Rev. Earth Planet. Sci. 46, 291–325. https://doi.org/10.1146/annurev-earth-082517-010146.

Schaltegger, U., Pettke, T., Audétat, A., Reusser, E., Heinrich, C.A., 2005. Magmatic-to-hydrothermal crystallization in the W-Sn mineralized Mole Granite (NSW, Australia). Chem. Geol. 220, 215–235. https://doi.org/10.1016/j.chemgeo.2005.02.018.

Schirmer, T., Ließmann, W., Macauley, C., Felfer, P., 2020. Indium and antimony distribution in a Sphalerite from the "Burgstaetter Gangzug" of the Upper Harz Mountains Pb-Zn Mineralization. Minerals 10, 1–19. https://doi.org/10.3390/min10090791.

Schwarz-Schampera, U., Herzig, P.M., 2002. Indium: Geology, mineralogy, and economics. Springer Science & Business Media.
Shaw, D.M., 1952. The geochemistry of indium. Geochim. Cosmochim. Acta 2, 185–206. https://doi.org/10.1016/0016-7037(52)90006-9.
Sheraton, J.W., Labonne, B., 1978. Petrology and geochemistry of acid igneous rocks of northeast Queensland. Geoscience Australia.
Sinclair, W.D., Kooiman, G.J.A., Martin, D.A., Kjarsgaard, I.M., 2006. Geology, geochemistry and mineralogy of indium resources at Mount Pleasant, New Brunswick, Canada. Ore Geol. Rev. 28, 123–145. https://doi.org/10.1016/j.oregeorev.2003.03.001.
Sláma, J., Košler, J., Condon, D.J., Crowley, J.L., Gerdes, A., Hanchar, J.M., Horstwood, M.S.A., Morris, G.A., Nasdala, L., Norberg, N., Schaltegger, U., Schoene, B., Tubrett, M.N., Whitehouse, M.J., 2008. Plešovice zircon — A new natural reference material for U-Pb and Hf isotopic microanalysis. Chem. Geol. 249, 1–35. https://doi.org/10.1016/j.chemgeo.2007.11.005.
Torró, C., Melgarejo, C., Tarrés, G., Campeny, A., Torres, M., Mollinedo, A., Arce-Burgoa, 2019. Indium Mineralization in the Volcanic Dome-Hosted Ánimas–Chocaya–Siete Suyos Polymetallic Deposit, Potosí, Bolivia. Minerals 9, 604. https://doi.org/10.3390/min9100604.
Valkama, M., Sundblad, K., Nygård, R., Cook, N., 2016. Mineralogy and geochemistry of indium-bearing polymetallic veins in the Sarvlaxviken area, Lovisa, Finland. Ore Geol. Rev. 75, 206–219. https://doi.org/10.1016/j.oregeorev.2015.12.001.
Vermeesch, P., 2018. IsoplotR: a free and open toolbox for geochronology. Geosci. Front. 9, 1479–1493. https://doi.org/10.1016/j.gsf.2018.04.001.
Vos, I.M.A., Bierlein, F.P., Phillips, D., 2007. The Palaeozoic tectono-metallogenic evolution of the northern Tasman Fold Belt System, Australia: interplay of subduction rollback and accretion. Ore Geol. Rev. 30, 277–296. https://doi.org/10.1016/j.oregeorev.2006.05.001.
Voudouris, P., Repstock, A., Spry, P.G., Frenzel, M., Mavrogonatos, C., Keith, M., Tarantola, A., Melfos, V., Tombros, S., Zhai, D., Cook, N.J., Ciobanu, C.L., Schaarschmidt, A., Rieck, B., Kolitsch, U., Falkenberg, J.J., 2022. Physicochemical constraints on indium-, tin-, germanium-, gallium-, gold-, and tellurium-bearing mineralizations in the Pefka and St Philippos polymetallic vein- and breccia-type deposits, Greece. Ore Geol. Rev. 140 https://doi.org/10.1016/j.oregeorev.2021.104348.
Walshe, J.L., Solomon, M., Whitford, D.J., Sun, S.S., Foden, J.D., 2011. The role of the mantle in the genesis of tin deposits and tin provinces of eastern Australia. Econ. Geol. 106, 297–305. https://doi.org/10.2113/econgeo.106.2.297.
Werner, T.T., Mudd, G.M., Jowitt, S.M., 2017. The world's by-product and critical metal resources part III: a global assessment of indium. Ore Geol. Rev. 86, 939–956. https://doi.org/10.1016/j.oregeorev.2017.01.015.
White, A.J.R., Allen, C.M., Beams, S.D., Carr, P.F., Champion, D.C., Chappell, B.W., Wyborn, D., Wyborn, L.A.I., 2001. Granite suites and supersuites of eastern Australia. Aust. J. Earth Sci. 48, 515–530. https://doi.org/10.1046/j.1440-0952.2001.00874.x.
Wiedenbeck, M., Allé, P., Corfu, F., Griffin, W.L., Meier, M., Oberli, F., Quadt, A., Roddick, J.C., Spiegel, W., 1995. Three natural zircon standards for U-Th-Pb, Lu-Hf, trace element and REE analyses. Geostand. Geoanalytical Res. 19, 1–23. https://doi.org/10.1111/j.1751-908X.1995.tb00147.x.
Withnall, I.W., Henderson, R.A., 2012. Accretion on the long-lived continental margin of northeastern Australia. Episodes 35, 166–176. 10.18814/epiiugs/2012/v35i1/016.
Xu, J., Cook, N.J., Ciobanu, C.L., Li, X., Kontonikas-Charos, A., Gilbert, S., Lv, Y., 2021. Indium distribution in sphalerite from sulfide–oxide–silicate skarn assemblages: a case study of the Dulong Zn–Sn–In deposit, Southwest China. Miner. Depos. 56, 307–324. https://doi.org/10.1007/s00126-020-00972-y.